

A human cardiopulmonary system model applied to the analysis of the Valsalva maneuver

K. Lu, J. W. Clark, Jr., F. H. Ghorbel, D. L. Ware and A. Bidani
AJP - Heart 281:2661-2679, 2001.

You might find this additional information useful...

This article cites 26 articles, 16 of which you can access free at:

<http://ajpheart.physiology.org/cgi/content/full/281/6/H2661#BIBL>

This article has been cited by 4 other HighWire hosted articles:

Multiscale Modeling of Cardiac Cellular Energetics

J. B. BASSINGTHWAIGHTE, H. J. CHIZECK, L. E. ATLAS and H. QIAN

Ann. N.Y. Acad. Sci., June 1, 2005; 1047 (1): 395-426.

[Abstract] [Full Text] [PDF]

Cerebral autoregulation and gas exchange studied using a human cardiopulmonary model

K. Lu, J. W. Clark Jr., F. H. Ghorbel, C. S. Robertson, D. L. Ware, J. B. Zwischenberger and A. Bidani

Am J Physiol Heart Circ Physiol, February 1, 2004; 286 (2): H584-601.

[Abstract] [Full Text] [PDF]

Addition of inspiratory resistance increases the amplitude of the slow component of O₂ uptake kinetics

J. Carra, R. Candau, S. Keslacy, F. Giolbas, F. Borrani, G. P. Millet, A. Varray and M. Ramonatxo

J Appl Physiol, June 1, 2003; 94 (6): 2448-2455.

[Abstract] [Full Text] [PDF]

Model simulations of cardiovascular changes at the onset of moderate exercise in humans

M. Elstad, K. Toska and L. Walloe

J. Physiol., September 1, 2002; 543 (2): 719-728.

[Abstract] [Full Text] [PDF]

Medline items on this article's topics can be found at <http://highwire.stanford.edu/lists/artbytopic.dtl> on the following topics:

Physiology .. Humans
Physiology .. Baroreflex
Medicine .. Valsalva's Maneuver
Medicine .. Pleura
Medicine .. Lungs
Medicine .. Airway

Updated information and services including high-resolution figures, can be found at:

<http://ajpheart.physiology.org/cgi/content/full/281/6/H2661>

Additional material and information about *AJP - Heart and Circulatory Physiology* can be found at:

<http://www.the-aps.org/publications/ajpheart>

This information is current as of March 26, 2006 .

AJP - Heart and Circulatory Physiology publishes original investigations on the physiology of the heart, blood vessels, and lymphatics, including experimental and theoretical studies of cardiovascular function at all levels of organization ranging from the intact animal to the cellular, subcellular, and molecular levels. It is published 12 times a year (monthly) by the American Physiological Society, 9650 Rockville Pike, Bethesda MD 20814-3991. Copyright © 2005 by the American Physiological Society. ISSN: 0363-6135, ESSN: 1522-1539. Visit our website at <http://www.the-aps.org/>.



A human cardiopulmonary system model applied to the analysis of the Valsalva maneuver

K. LU,¹ J. W. CLARK, JR.,¹ F. H. GHORBEL,¹ D. L. WARE,² AND A. BIDANI²

¹*Dynamical Systems Group, Rice University, Houston 77005; and* ²*Department of Internal Medicine, University of Texas Medical Branch, Galveston, Texas 77555*

Received 12 March 2001; accepted in final form 13 August 2001

Lu, K., J. W. Clark, Jr., F. H. Ghorbel, D. L. Ware, and A. Bidani. A human cardiopulmonary system model applied to the analysis of the Valsalva maneuver. *Am J Physiol Heart Circ Physiol* 281: H2661–H2679, 2001.—Previous models combining the human cardiovascular and pulmonary systems have not addressed their strong dynamic interaction. They are primarily cardiovascular or pulmonary in their orientation and do not permit a full exploration of how the combined cardiopulmonary system responds to large amplitude forcing (e.g., by the Valsalva maneuver). To address this issue, we developed a new model that represents the important components of the cardiopulmonary system and their coupled interaction. Included in the model are descriptions of atrial and ventricular mechanics, hemodynamics of the systemic and pulmonic circulations, baroreflex control of arterial pressure, airway and lung mechanics, and gas transport at the alveolar-capillary membrane. Parameters of this combined model were adjusted to fit nominal data, yielding accurate and realistic pressure, volume, and flow waveforms. With the same set of parameters, the nominal model predicted the hemodynamic responses to the markedly increased intrathoracic (pleural) pressures during the Valsalva maneuver. In summary, this model accurately represents the cardiopulmonary system and can explain how the heart, lung, and autonomic tone interact during the Valsalva maneuver. It is likely that with further refinement it could describe various physiological states and help investigators to better understand the biophysics of cardiopulmonary disease.

cardiopulmonary modeling; ventricular interaction; closed-loop hemodynamics; baroreflex control; airway mechanics; gas exchange

THE DIAGNOSIS AND TREATMENT of cardiopulmonary disease may be improved by using mathematical models of the cardiovascular and pulmonary systems. With this in mind, we developed a model of the cardiopulmonary system of the normal human subject that not only represents the system accurately but also predicts its response to a variety of commonly used diagnostic procedures. To our knowledge, this is the first example of a truly integrative model of the cardiopulmonary system.

Recently, our group (5, 25) developed a multicompartiment model of the canine circulation. We have now modified and extended this cardiovascular model to

encompass human heart mechanics, a circulatory loop, baroreflex control of arterial pressure, airway mechanics, and gas transport at the alveolar-capillary membrane.

Distributed circulatory models of the systemic and pulmonic circulations have been developed (1, 3, 12, 37). However, the mechanics of the lung and airways were not detailed in any of these, and the heart was modeled rather simply. The gas exchange at the alveolar-capillary membrane (an obvious link between cardiovascular and pulmonary system) was considered only in the model of Hardy et al. (12). Of these models, baroreflex control of arterial pressure was included only in the work of Ursino et al. (37).

Distributed airway mechanics models [e.g., Elad et al. (7) and Lambert et al. (16)] can be too complex for a combined cardiopulmonary model, making lumped lower-order compartment models [such as that of Lutchen et al. (19)] preferred. The lumped compartment model we (18) developed describes ventilation, perfusion, mechanics, and gas transport over the full range of normal lung volumes. A modified version of this model was used in the current study.

Our heart model was based on our previous work in dogs (5, 25). The parameters of that model were adjusted to better fit the flow, volume, and temporal relationships of the human cardiac cycle. Similar adjustments were made in the systemic and pulmonic component models of the canine circulatory loop (25). The resulting model is of intermediate complexity and simulates pressure, volume, and flow distribution of the human subject in the supine position.

To better simulate the cardiovascular response to perturbation, we added nonlinear descriptions of the venous system and a description of how the baroreflexes influence heart rate, myocardial contractility, and vasomotor tone. We based our baroreceptor control model on the work of Spickler et al. (35) and Wesseling et al. (38) and included descriptions of both parasympathetic (vagal) and sympathetic pathways.

Our new lung model combines models previously developed by our group, namely, an airway mechanics model [from Athanasiades et al. (2)] and a gas ex-

Address for reprint requests and other correspondence: J. W. Clark, Dept. of Electrical and Computer Engineering, Rice Univ., 6100 Main St., Houston, TX 77005 (E-mail: jwc@ece.rice.edu).

The costs of publication of this article were defrayed in part by the payment of page charges. The article must therefore be hereby marked "advertisement" in accordance with 18 U.S.C. Section 1734 solely to indicate this fact.



change model [modified from Liu et al. (18)]. It characterizes the nonlinear resistive-compliant properties of the airways and the nonlinear pressure-volume characteristics of the lung. A distributed pulmonary circulatory model containing 35 contiguous capillary segments characterizes gas exchange at the alveolar-capillary membrane and yields good fits to expired O₂ and CO₂ data measured at the mouth.

This integrated cardiopulmonary model describes heart-lung interactions and the timing of baroreflex changes in heart rate, myocardial contractility, and vasomotor tone. Its parameters fit available cardiovascular and pulmonary data obtained during tidal breathing and can predict the responses to large-scale perturbations in pleural pressure, such as those occurring in the forced vital capacity and Valsalva maneuvers.

Glossary

Activation functions

$e(t)$	Time-varying activation function
$e_a(t)$	Activation function of the atrium
$e_v(t)$	Activation function of the ventricle

Airflows

\dot{Q}_{CA}	Airflow from collapsible airways to alveolar region
\dot{Q}_{DC}	Airflow from upper supported airway to collapsible airway
\dot{Q}_{ED}	Airflow from environment to upper supported airway

Blood flows

\dot{Q}_{Ao}	Aortic flow
\dot{Q}_{PA}	Pulmonary arterial flow

Compliances

$C_{Ao,P}$	Aortic root compliance
$C_{Ao,D}$	Distal aortic compliance
C_{PA}	Pulmonary artery compliance
$C_{PA,D}$	Distal pulmonary artery compliance
C_{PC}	Pulmonary capillary compliance
C_{PV}	Pulmonary venous compliance
$C_{SA,D}$	Distal systemic artery compliance
C_{SC}	Systemic capillary compliance

Constants and scaling parameters

a	Time constant
a_{min}	Dimensionless constant
a_x	Normalized frequency offset
A_i	Parameter of activation function of the heart
b_{min}	Dimensionless constant
b_x	Dimensionless constant
B_i	Parameter of activation function of the heart
C_i	Parameter of activation function of the heart
C_{LT}	Lung tissue elastic constant

D_0	Volume parameter
D_1	Stressed pressure offset
D_2	Unstressed pressure offset
h_1	Constant
h_2	Constant
h_3	Constant
h_4	Constant
h_5	Constant
h_6	Constant
K	Gain
K_1	Stressed scaling pressure
K_2	Unstressed scaling pressure
K_a	Scaling parameter
K_b	Scaling parameter
K_c	Scaling parameter
K_{p1}	Constant scaling parameter
K_{p2}	Constant scaling parameter
K_r	Resistance scaling factor
K_R	Resistance scaling factor
K_v	Scaling factor for pressure
λ	Diastolic elastance coefficient
τ_p	Passive exponential constant
τ_x	Time constant

Gas diffusion and flux

$C_{bi}^{(j)}$	Gas species i blood concentration in the j th capillary
D_{Li}	Diffusion capacity for the i th gas species
D_{L,CO_2}	Lung diffusion capacity of CO ₂
D_{L,N_2}	Lung diffusion capacity of N ₂
D_{L,O_2}	Lung diffusion capacity of O ₂
Φ_{tot}	Total gas flux rate

Inertances

$L_{Ao,D}$	Distal aortic inertance
$L_{Ao,P}$	Aortic root inertance
L_{PA}	Pulmonary arterial inertance

Neural control

F_{con}	Normalized sympathetic efferent discharge frequency controlling contractility
$F_{Hr,S}$	Normalized sympathetic controlling HR frequency
$F_{Hr,V}$	Normalized vagal controlling HR frequency
F_{symp}	Sympathetic discharge frequency
F_{vagus}	Vagal discharge frequency
F_{vaso}	Normalized sympathetic efferent discharge frequency controlling vasomotor tone
F_x	Discharge frequency
x	Generic output index representing heart rate, contractility, or vasomotor tone
N_1	Baroreceptor firing frequency
N_2	Derivative of baroreceptor firing frequency
N_{con}	Sympathetic discharge at central nervous system controlling contractility



$N_{Hr,S}$	Sympathetic discharge at central nervous system controlling heart rate	P_{CO_2}	Partial pressure of CO_2
$N_{Hr,V}$	Vagal discharge at central nervous system controlling heart rate	P_{D_i}	Partial pressure of gas species i in the upper airway
$N(s)$	Laplace transform of $N(t)$	P_D	Pressure in the lung dead space
$N(t)$	Baroreceptor discharge frequency	P_{D,CO_2}	CO_2 partial pressure in the lung dead space
N_{vaso}	Sympathetic discharge at central nervous system controlling vasomotor tone	P_{D,O_2}	O_2 partial pressure in the lung dead space
$N_{vaso}(s)$	Laplace transform of N_{vaso}	P_{EL}	Lung elastic recoil pressure
$N_{x,0}$	Base frequency	$P_{ES}(V)$	End-systolic pressure
$N_x(t)$	Discharge frequency of neural pathways of the central nervous system	$P_{b_i}^{(j)}$	Partial pressure of gas species i in the j th capillary

Physiology

Ao_D	Distal aorta
Ao_P	Proximal aorta
BR	Baroreceptor element
CNS	Central nervous system
LA	Left atrium
LV	Left ventricle
LVF	Left ventricular free wall
PA	Pulmonary arterioles
PA_D	Distal pulmonary arterioles
PA_P	Proximal pulmonary arterioles
PC	Pulmonary capillaries
PCD	Pericardium
PV	Pulmonary veins
RA	Right atrium
RV	Right ventricle
RVF	Right ventricular free wall
SA_D	Distal systemic arterioles
SA_P	Proximal systemic arterioles
SC	Systemic capillaries
SPT	Septum
SV	Systemic veins
VC	Vena cava

Pressures

P_0	Diastolic pressure magnitude
P_{atm}	Atmospheric pressure
$P_{atm,i}$	Partial pressure of gas species i in the atmosphere
P_{A_i}	Partial pressure of gas species i in the small airway
P_A	Alveolar pressure
P_{A,CO_2}	Alveolar CO_2 partial pressure
P_{A,O_2}	Alveolar O_2 partial pressure
P_{Ao}	Aortic arch pressure
P_{b,CO_2}	CO_2 partial pressure in the blood
P_{b,O_2}	O_2 partial pressure in the blood
P_{C_i}	Partial pressure of gas species i in the middle airway
P_C	Pressure in the lumen of the midairway segment
P_{C,CO_2}	CO_2 partial pressure in the collapsible airway
P_{C,O_2}	O_2 partial pressure in the collapsible airway
P_{CW}	Recoil pressure of the chest wall

P_{D_i}	Partial pressure of gas species i in the upper airway
P_D	Pressure in the lung dead space
P_{D,CO_2}	CO_2 partial pressure in the lung dead space
P_{D,O_2}	O_2 partial pressure in the lung dead space
P_{EL}	Lung elastic recoil pressure
$P_{ES}(V)$	End-systolic pressure
$P_{b_i}^{(j)}$	Partial pressure of gas species i in the j th capillary
P_{LA}	Left atrial pressure
P_{LV}	Left ventricular pressure
P_{mus}	Pressure of the respiratory muscles
P_{O_2}	Partial pressure of O_2
P_{PL}	Pleural pressure
P_{SA}^a	Systemic arterial pressure in the active state
P_{SA}^p	Systemic arterial pressure in the passive state
P_{SV}	Transmural pressure of systemic veins
P_{TM}	Transmural pressure of collapsible midairway
P_{VC}	Transmural pressure of the vena cava

Resistances

R_0	Offset parameter
$R_{Ao,P}$	Aortic root flow resistance
$R_{Ao,D}$	Distal aortic flow resistance
R_C	Resistance of collapsible midairway
R_{COR}	Coronary flow resistance
R_{CRB}	Cerebral flow resistance
R_{LA}	Left atrial flow resistance
R_{LT}	Lung tissue resistive constant
R_M	Mitral valve flow resistance
R_{PA}	Pulmonary arteriolar flow resistance
$R_{PA,D}$	Distal pulmonary arterial flow resistance
$R_{PA,P}$	Proximal pulmonary arterial flow resistance
R_{PC}	Resistance of pulmonary capillaries
$R_{PC,0}$	Magnitude of pulmonary capillary resistance
R_{PS}	Pulmonary shunt flow resistance
R_{PV}	Pulmonary venous flow resistance
R_{RA}	Right atrial flow resistance
R_S	Small airways resistance
R_{SA}	Resistance of systemic arteries
$R_{SA,D}$	Systemic arteriolar flow resistance
R_{SC}	Systemic capillary flow resistance
R_{SV}	Systemic venous flow resistance
R_{TAo}	Viscoelastic resistance of proximal aorta wall
$R_{TAo,D}$	Viscoelastic resistance of distal aorta wall
R_{TA}	Tricuspid valve flow resistance
R_{TPA}	Pulmonary artery wall viscoelastic resistance
R_{uaw}	Upper supported airway resistance
R_{VC}	Resistance of the vena cava



Variables and measurements

E_{ES}	End-systolic elastance
EDPVR	End-diastolic pressure-volume relationship
ESPVR	End-systolic pressure-volume relationship
FRC	Functional residual capacity
FVC	Forced vital capacity
i	Gas species (O_2 , CO_2 , or N_2)
j	Number of a specific capillary in a series
N_{seg}	Number of capillary segments
P-V	Pressure-volume (relationship)
s	Laplace variable
STPD	Standard temperature, pressure, dry weight
t	Time
TLC	Total lung capacity
$v_{2b}^{(j)}$	Blood flow velocity in the j th capillary
z	Length coordinate of the pulmonary capillary

Volumes

V_0	Unstressed volume
V_A	Alveolar volume
$V_{A,max}$	Maximal alveolar volume
V_C	Collapsible airway volume
V_{CW}	Chest wall volume
V_D	Systolic volume offset
V_{ED}	End-diastolic volume
V_{ES}	End-systolic volume
$V_b^{(j)}$	Blood volume contained in the j th capillary
V_L	Lung volume
V_{LV}	Left ventricular volume
V_{max}	Maximal volume
V_{min}	Minimum volume
V_{PC}	Blood volume of pulmonary capillaries
$V_{PC,max}$	Maximal blood volume of pulmonary capillaries
V_{SA}	Blood volume of systemic arteries
$V_{SA,0}$	Minimal volume of systemic arteries
$V_{SA,max}$	Maximal lumen volume of systemic arteries
V_{SV}	Luminal volume of systemic veins
V_{VC}	Luminal volume of the vena cava
V_{VE}	Viscoelastic volume

MODEL DEVELOPMENT

Ventricular Model

Our ventricular model is based on the work of Chung et al. (5), wherein each ventricular compartment is characterized by a time-varying elastance function (Tables 1–3). The elastance function is developed by three curves, as established in Ref. 5, namely, the end-systolic P-V relationship (ESPVR), the end-diastolic P-V relationship (EDPVR), and a time-varying activation function [$e(t)$]. The activation function $e(t)$ consists of a series of Gaussian curves and serves to produce a smooth

Table 1. Parameter values of the ventricular model

Parameters	LVF	RVF	PCD
E_{ES} , mmHg/ml	4.3	0.6	N/A
P_0 , mmHg	1.7	0.67	0.5
V_0 , ml	25	25	200
V_D , ml	40	40	N/A
λ , ml^{-1}	0.015	0.015	0.005

For abbreviations, see *Glossary* and text.

transition between the EDPVR and the ESPVR. A detailed description of the ventricular model can be found in Ref. 5.

Circulatory Model

The general framework of our human circulatory loop model (Fig. 1 and Table 4) is similar to that of Olansen et al. (25) with certain extensions and modifications. We included 1) nonlinear P-V relationships to describe the peripheral venous system, 2) a nonlinear collapsible description of the P-V relationship for the vena cava, and 3) separate descriptions of baroreceptor-mediated control of heart rate, myocardial contractility, and vasomotor tone.

Nonlinear P-V Characteristics of Systemic Veins and the Vena Cava

Systemic veins. The nonlinear P-V relationship of veins has been modeled previously by Kresch (15) and by Snyder and Rideout (34). As volume increases, the vessels stiffen. The resulting P-V curve can be represented as follows

$$P_{SV} = -K_v \times \log \left(\frac{V_{max}}{V_{SV}} - 0.99 \right) \quad (1)$$

where P_{SV} and V_{SV} are the transmural pressure and luminal volume of systemic veins, K_v is a scaling factor (in mmHg), and V_{max} is the maximal volume (in ml) of the lumped systemic veins (Table 5).

Vena cava. Under some conditions, the vena cava may collapse. For example, when pleural pressure is greater than the luminal pressure of the vena cava, total caval volume decreases substantially, and the resistance to flow is increased. To account for this, we described the P-V relationship as follows

$$\text{if } V_{VC} \geq V_0, \text{ then } P_{VC} = D_1 + K_1 \times (V_{VC} - V_0) \quad (2)$$

$$\text{if } V_{VC} < V_0, \text{ then } P_{VC} = D_2 + K_2 \times e^{(V_{VC}/V_{min})} \quad (3)$$

where P_{VC} and V_{VC} denote the transmural pressure and luminal volume of the vena cava, respectively, V_0 is the unstressed volume, and V_{min} is the minimum volume. We adjusted the parameters K_1 , K_2 , D_1 , and D_2 to produce P-V curves similar to those used in the human venous model of Snyder and Rideout (34).

Table 2. Parameter values of the atrial model

Parameters	LA	RA
E_{ES} , mmHg/ml	0.2	0.2
P_0 , mmHg	0.5	0.5
V_0 , ml	20	20
V_D , ml	20	20
λ , ml^{-1}	0.025	0.025

For abbreviations, see *Glossary* and text.

Table 3. Parameter values for the activation function

Parameters	$e_v(t)$				$e_a(t)$
	$i = 1$	$i = 2$	$i = 3$	$i = 4$	
A_i	0.3	0.35	0.5	0.55	0.9
B_i, s^2	0.045	0.035	0.037	0.036	0.018
C_i, s	0.175	0.23	0.275	0.3	0.025

Parameter A_i is dimensionless. For abbreviations, see *Glossary* and text.

The resistance of the vena cava (R_{VC}) is a nonlinear function of its luminal blood volume (V_{VC}) according to the following equation

$$R_{VC} = K_R \times \left(\frac{V_{max}}{V_{VC}} \right)^2 + R_0 \quad (4)$$

where K_R is a scaling factor (in $mmHg \cdot s \cdot ml^{-1}$), V_{max} denotes the maximum volume, and R_0 is an offset parameter (in $mmHg \cdot s \cdot ml^{-1}$) (Table 5).

Arterial Baroreflex Control

Our previous study (25) did not consider baroreflex control of heart rate, myocardial contractility, and vasomotor tone. We have now included lumped characterizations of the baroreceptors and their reflex pathways in the present study, according to the general structure used by Wesseling et al. (38).

Baroreceptors. Figure 2 includes four functional blocks that represent the baroreceptor, the central nervous system (CNS), the efferent pathways, and the effector organ. The input to the baroreceptor element (BR) is central arterial pressure [aortic arch pressure (P_{Ao})], and the output [$N(t)$] is the instantaneous firing frequency of the BR. Following Spickler et al. (35), we characterized the input-output relationship in terms of the following transfer function

$$\frac{N(s)}{P_{Ao}(s)} = \frac{K \times (1 + 0.036s)}{(1 + 0.0018s)(1 + as)} \quad \text{where } a < 0.0018 \quad (5)$$

Table 4. Nominal parameter values in the systemic and pulmonic circulations

Parameters	Values
<i>Resistances, mmHg·s·ml⁻¹</i>	
$R_{Ao,D}$	0.015
$R_{Ao,P}$	0.005
R_{COR}	30
R_{CRB}	10
R_{LA}	0.01
R_M	0.008
R_{PA}	0.005
$R_{PA,D}$	0.005
$R_{PA,P}$	0.002
R_{PC}	0.008
R_{PS}	4.5
R_{PV}	0.008
R_{RA}	0.05
$R_{SA,D}$	0.8
R_{SC}	0.6
R_{SV}	0.17
R_{TAo}	0.06
$R_{TAo,D}$	0.0125
R_{TC}	0.015
R_{TPA}	0.02
<i>Compliances, ml/mmHg</i>	
$C_{Ao,D}$	0.2
$C_{Ao,P}$	1.6
C_{PA}	0.5
$C_{PA,D}$	0.05
$C_{PA,P}$	0.8
C_{PC}	1.0
C_{PV}	4.0
$C_{SA,D}$	0.069
C_{SC}	0.2
<i>Inertances, mmHg·s²·ml⁻¹</i>	
$L_{Ao,D}$	0.0017
$L_{Ao,P}$	0.01226
L_{PA}	0.00018

For abbreviations, see *Glossary* and text.

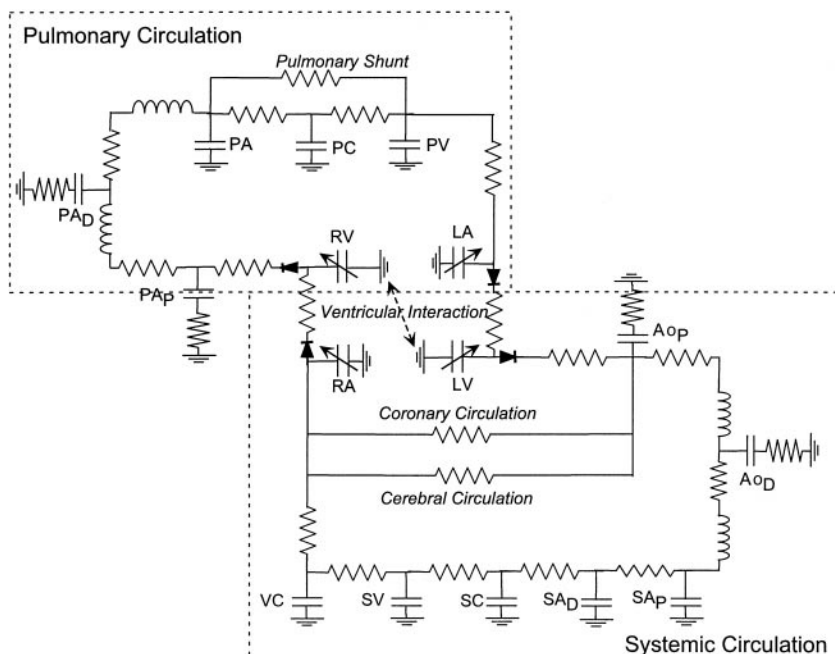


Fig. 1. A hydraulic equivalent representation of the closed-loop circulatory model. For abbreviations, see *Glossary*.

Table 5. Parameter values for nonlinear P-V curves of systemic veins and the vena cava

Parameters	Values
<i>Systemic Veins</i>	
K_v , mmHg	40
V_{max} , ml	3,500
<i>Vena Cava</i>	
D_1 , mmHg	0.0
D_2 , mmHg	-5.0
K_1 , mmHg	0.15
K_2 , mmHg	0.4
K_R , mmHg·s·ml ⁻¹	0.001
R_0 , mmHg·s·ml ⁻¹	0.025
V_0 , ml	130
V_{max} , ml	350
V_{min} , ml	50

For abbreviations, see *Glossary* and text.

The corresponding differential equation is as follows

$$0.0018a \frac{d^2N(t)}{dt^2} + (0.0018 + a) \frac{dN(t)}{dt} + N(t) = K \left[P_{Ao}(t) + 0.036K \frac{dP_{Ao}(t)}{dt} \right] \quad (6)$$

where K is the gain and a is a time constant [35].

Central nervous system. The medullary cardiovascular control center is modeled in terms of four noninteracting pathways, each characterized by filtering, gain, and a delay as per the modeling concept of Wessling et al. (38). One vagal (fast) and one sympathetic (slow) pathway each controls heart rate, whereas two other sympathetic pathways control myocardial contractility and vasomotor tone. The fast vagal pathway has a 0.2-s delay, whereas each sympathetic pathway has a 3-s delay.

Efferent pathways. We described each efferent pathway according to the following generic equation in normalized form (Table 6)

$$F_x(t) = a_x + \frac{b_x}{e^{\tau_x[N_x(t) - N_{x,0}]} + 1.0} \quad (7)$$

The generic parameter x represents heart rate, contractility, or vasomotor tone. The parameters τ_x and $N_{x,0}$ were fitted to the representative data. This equation provides a sigmoidal input-output relationship (threshold and saturation) between central neuron activity (output of central delay box) and the discharge frequency of the particular motor neuron (6, 11, 22, 29, 35).

Because increases in BR firing frequency increase vagal discharge frequency, τ_x in the vagal efferent pathway is negative, producing a monotonically increasing input-output relationship for the linear part of the curve (Fig. 2). Sympathetic pathways use positive τ_x values, because BR and sympathetic discharge frequencies change in opposite directions. Figure 2 shows that the discharge frequency (F_x) of each efferent pathway inputs to the final block of the diagram, which contains characterization of the input-output response of the effector organ itself (the heart or vessel).

Effector organs. Heart rate is controlled by vagal and sympathetic neural activity and has been characterized by Sunagawa as a three-dimensional response surface [36]. We developed the following equation to characterize the human heart rate response surface to vagal and sympathetic input (Table 7)

$$HR = h_1 + h_2 \times F_{HR,S} - h_3 \times F_{HR,S}^2 - h_4 \times F_{HR,V} + h_5 \times F_{HR,V}^2 - h_6 \times F_{HR,V} \times F_{HR,S} \quad (8)$$

where HR (in beats/min) represents heart rate, $F_{HR,V}$ and $F_{HR,S}$ are the normalized vagal and sympathetic frequencies, and h_1-h_6 are constants. This formula generates a normalized heart rate response surface analogous to that of Sunagawa et al. (36).

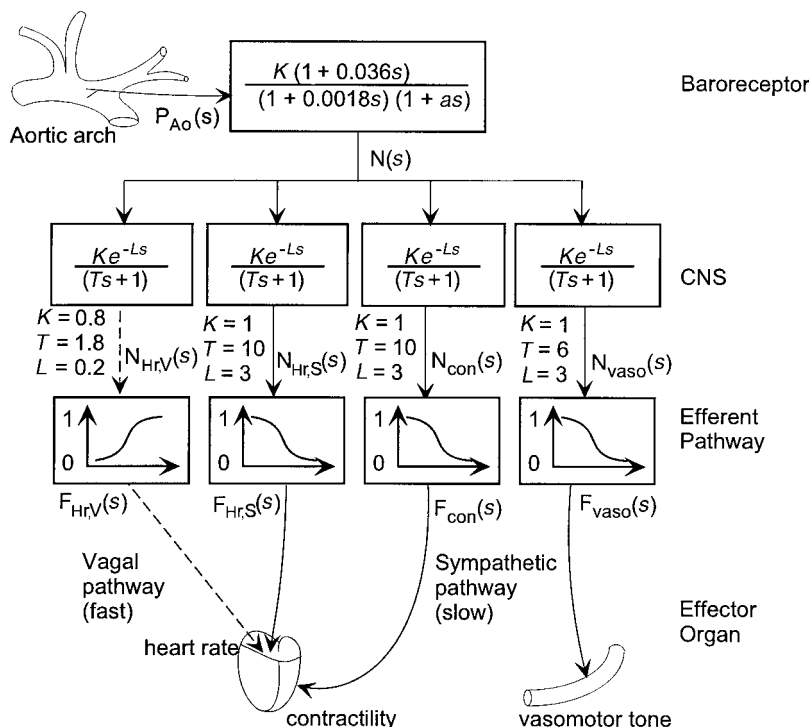


Fig. 2. Block diagram of baroreflex control of arterial pressure. A fast vagal (dashed arrow) pathway and 3 slow sympathetic pathways are included to control heart rate, myocardial contractility, and vasomotor tone. The overall control scheme is based on the modeling concept of Wessling et al. (38). For abbreviations, see text.

Table 6. Parameter values for the baroreflex pathway

Parameters	Vagal	Sympathetic		
		Heart rate	Contractility	Vasomotor tone
a_x	0	0.3	0.3	0.3
b_x	1.0	0.7	0.7	0.7
$N_{x,0}$, Hz	110	100	110	110
τ_x , s	-0.04	0.09	0.04	0.04

Parameters a_x and b_x are dimensionless. For abbreviations, see Glossary and text.

In our study, the heart period (calculated as 60/HR, in s) is explicitly determined by the vagal-sympathetic mechanism according to Eq. 8, and the systolic period is mediated by the sympathetic frequency (Fig. 3). The diastolic filling time is the difference between the two and is thus controlled indirectly.

Greater sympathetic tone increases myocardial elastance and shortens ventricular systole. Therefore, we modified the ventricular activation function to describe the change in ventricular elastance [$e(t)$] as a function of sympathetic efferent discharge frequency (F_{con}) (see Fig. 3).

A rise in F_{con} increases maximum elastance and shortens the systolic period. The expression for the end-systolic P-V relationship [$P_{ES}(V)$] becomes (notation from Ref. 25 and Table 1)

$$P_{ES}(V) = \alpha(F_{con}) \times E_{ES} \times (V - V_D) \quad (9)$$

and the activation function [$e_v(t)$] becomes

$$e_v(t, F_{con}) \equiv \sum_{i=1}^n A_i e^{-\frac{1}{2} \left(\frac{b(F_{con}) \times t - C_i}{B_i} \right)^2} \quad (10)$$

where

$$\alpha(F_{con}) = \alpha_{min} + K_a \times F_{con} \quad (11)$$

$$b(F_{con}) = b_{min} + K_b \times F_{con} \quad (12)$$

Here, α_{min} and b_{min} are dimensionless constants representing the minimum values of the functions α and b , respectively, and K_a and K_b are scaling parameters.

Arteries and arterioles are the major resistance vessels. When their smooth muscle constricts, lumen diameter decreases, axial resistance to flow increases, and the muscle wall stiffens. Therefore, a change in vasomotor tone involves a change in both axial resistance and in wall compliance. We transformed the passive and fully activated length-tension relationships previously described by Gore and Davis (10) into an equivalent P-V relationship for a cylindrical vessel. Figure 4 shows the passive and fully activated P-V curves used in our model, which are represented as follows. Fully activated

$$P_{SA}^a(V_{SA}) = K_c \times \log \left(\frac{V_{SA} - V_{SA,0}}{D_0} + 1 \right) \quad (13)$$

and passive

$$P_{SA}^p(V_{SA}) = K_{p1} \times e^{\tau_p \times (V_{SA} - V_{SA,0})} + K_{p2} \times (V_{SA} - V_{SA,0})^2 \quad (14)$$

where P_{SA}^a and P_{SA}^p represent the arterial pressures in the fully activated and passive states, respectively, V_{SA} is the blood volume contained in systemic arteries, and $V_{SA,0}$ (in ml) is the minimal volume. We assume $V_{SA} \geq V_{SA,0}$ in Eqs. 13 and 14. K_c , K_{p1} , and K_{p2} (in mmHg) are constant scaling parameters, D_0 (in ml) is a volume parameter, and τ_p (in ml^{-1}) is constant. During sympathetic stimulation, the compliance of the vessel is characterized by Eq. 13; when the

Table 7. Nominal parameter values for the effector organs in the baroreflex model

Parameters	Values
<i>Heart Rate</i>	
h_1	35
h_2	140
h_3	40
h_4	32
h_5	10
h_6	20
<i>Contractility</i>	
a_{min}	-2
b_{min}	0.7
K_a	5
K_b	0.5
<i>Vasomotor Tone</i>	
D_0 , ml	50
K_c , mmHg	1,000
K_{p1} , mmHg	0.03
K_{p2} , mmHg/ml ²	0.2
K_r , mmHg·s·ml ⁻¹	0.04
$V_{SA,0}$, ml	210
$V_{SA,max}$, ml	250
τ_p , ml ⁻¹	0.1

Values for heart rate and contractility are dimensionless. For abbreviations, see text.

sympathetic tone is abolished, the compliance of vessel wall is described by Eq. 14. The normalized sympathetic efferent frequency (F_{vaso}) serves as a scaling factor for the transition between these states

$$P_{SA}(V_{SA}) = F_{vaso} \times P_{SA}^a(V_{SA}) + (1 - F_{vaso}) \times P_{SA}^p(V_{SA}) \quad (15)$$

Axial resistance is also affected by sympathetic activity. Resistance (R_{SA} ; in mmHg·s·ml⁻¹) and sympathetic efferent frequency (F_{vaso}) are related by

$$R_{SA} = K_r \times e^{4 \times F_{vaso}} + K_r \times \left(\frac{V_{SA,max}}{V_{SA}} \right)^2 \quad (16)$$

The first term is regulated by the sympathetic frequency and the second term is a function of lumen volume (V_{SA}). $V_{SA,max}$

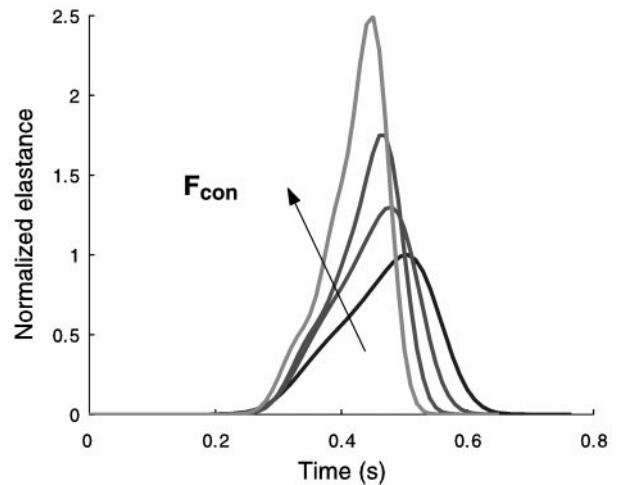


Fig. 3. Model representation of the sympathetically regulated activation function $e(t)$. Four different levels of contractility corresponding to different sympathetic efferent frequencies (F_{con}) are shown.

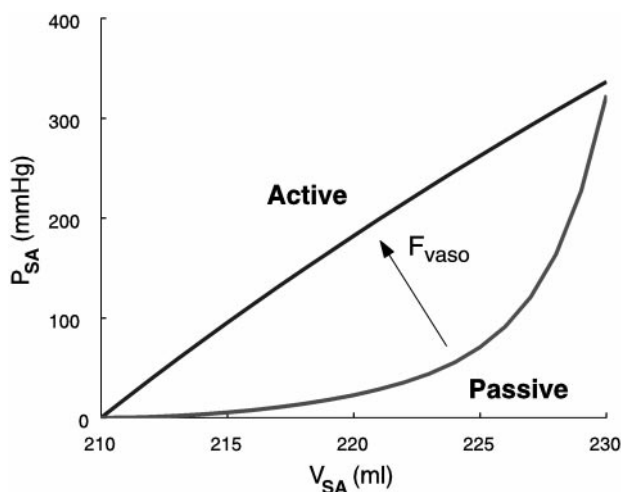


Fig. 4. Active and passive P-V curves of systemic arteries. P_{SA} and V_{SA} represent the pressure and volume in the systemic arteries. F_{vaso} is the normalized sympathetic discharge frequency controlling the vasomotor tone.

is the maximal lumen volume and K_r (in mmHg) is a pressure scaling constant.

Airway/Lung Mechanics Model

The pulmonary portion of our cardiopulmonary model combines two models previously developed. One focuses on airway/lung mechanics (2) and the other focuses on gas exchange (18). Figure 5 shows an equivalent pneumatic circuit model of the airways and lung of the normal human. The lung mechanics model (2) includes nonlinear characterizations of airway resistance, airway and chest wall compliance, and lung tissue viscoelasticity. This particular model (2) has also been used in a related context to analyze the “work of breathing” during clinical breathing maneuvers [see Athanasiades et al. (2) for details].

In the supine human, the lungs and their airways are subject to the same time-varying intrathoracic pleural pressure (P_{PL}). Figure 5 indicates that this pressure is generated

by the respiratory muscles (P_{mus}) and the recoil pressure of the chest wall (P_{CW}). Measured P_{PL} is also the driving pressure for our airway mechanics model. The upper airway is assumed rigid and is characterized by a nonlinear flow-dependent resistor (Rohrer resistor). The midairways are assumed collapsible and are characterized by a nonlinear volume-dependent resistance [$R_C(V_C)$] and a nonlinear P-V relationship [$P_{TM}(V_C)$], where V_C is the collapsible segment volume (Fig. 5). Pressure in the lumen of the midairway segment of the model is denoted as P_C , and the transmural pressure across the wall is denoted as P_{TM} . P_A is the alveolar pressure and P_{EL} is the lung elastic recoil pressure. Small airways resistance (R_S) is characterized as a nonlinear function of the alveolar volume (V_A).

From an analysis of the pneumatic circuit according to Newton’s first law

$$P_A = P_{EL} + R_{LT}\dot{V}_A + P_{PL} \quad (17)$$

$$P_C = P_{TM} + P_{PL} \quad (18)$$

$$P_{PL} = P_{CW} + P_{mus} \quad (19)$$

The component air flows (in ml/s) in the airway system are computed according to the equations below, which are derived from the continuity equation applied to each node of the pneumatic network. The resulting differential equations are as follows

$$\dot{Q}_{CA} = \frac{P_C - P_A}{R_S} \quad (20)$$

$$\dot{Q}_{DC} = \frac{P_D - P_C}{R_C} \quad (21)$$

$$\dot{Q}_{CA} = \frac{P_{atm} - P_D}{R_{uaw}} = \dot{Q}_{ED} \quad (22)$$

As such, the rate of the volume changes in the airway may be written as follows

$$\dot{V}_C = \dot{Q}_{DC} - \dot{Q}_{CA} \quad (23)$$

$$\dot{V}_A = \dot{Q}_{CA} - \Phi_{tot} \quad (24)$$

where Φ_{tot} denotes the total gas flux rate (in ml/s) of all gaseous species across the alveolar-capillary membrane, as given by Eq. 31.

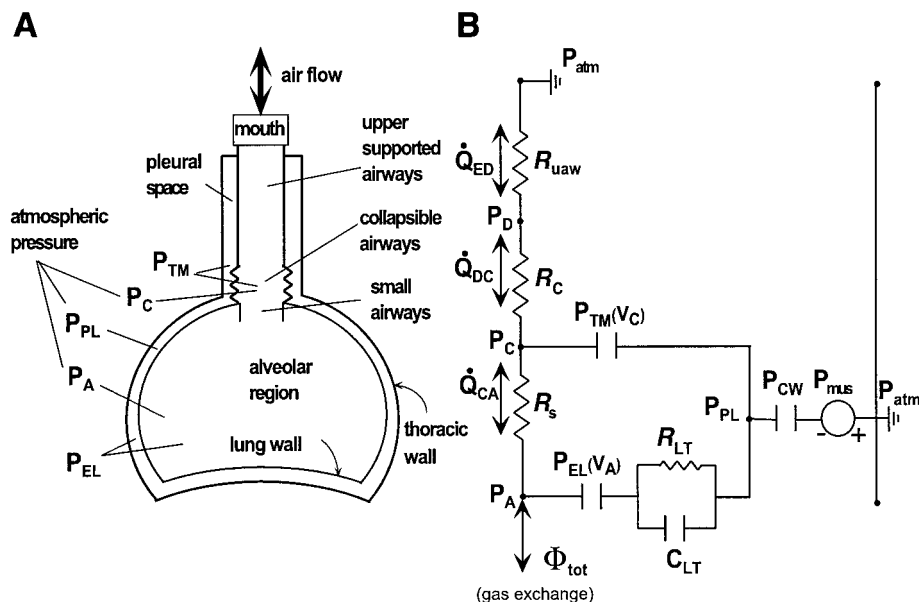


Fig. 5. Airway/lung mechanics model. A: components of airway mechanics, pulmonary circulation, and gas exchange. B: equivalent pneumatic circuit representation of airway/lung mechanics and gas exchange [modified from Athanasiades et al. (2)]. For abbreviations, see Glossary and text.



Gas Exchange Model

Gas exchange between air and blood occurs across the alveolar-capillary membrane. For modeling purposes, we assumed 1) inspired air is instantly warmed to body temperature and saturated with water vapor, 2) gaseous content obeys the ideal gas law, 3) blood is characterized as a uniform homogeneous medium, and 4) reactions between the gaseous species and blood are assumed to equilibrate instantaneously. The empirical O₂ and CO₂ dissociation curves relate the content of each species with their corresponding partial pressures in blood. The diffusing capacity for the *i*th gaseous species (D_{L*i*}) characterizes its diffusion across the alveolar-capillary membrane. O₂ is taken up by the blood, CO₂ is removed, and N₂ diffuses either way depending on the direction of their instantaneous partial pressure gradients.

The species conservation law is applied to inspiration and expiration. Inspiration can be described as follows

dP_{D*i*}/dt = 1/V_D (Q_{ED}P_{atm,*i*} - Q_{DC}P_{D*i*}) (25)

dP_{C*i*}/dt = 1/V_C (Q_{DC}P_{D*i*} - Q_{CA}P_{C*i*} - P_{C*i*} dV_C/dt) (26)

dP_{A*i*}/dt = 1/V_A { Q_{CA}P_{C*i*} - P_{A*i*} dV_A/dt - sum_{j=1}^{N_{seg}} [D_{L*i*}[P_{A*i*} - P_{b*i*}^(j)]ΔV_{PC}^j / V_{PC} } (27)

and expiration can be described as follows

dP_{D*i*}/dt = 1/V_D (Q_{ED}P_{D*i*} - Q_{DC}P_{C*i*}) (28)

dP_{C*i*}/dt = 1/V_C (Q_{DC}P_{C*i*} - Q_{CA}P_{A*i*} - P_{C*i*} dV_C/dt) (29)

dP_{A*i*}/dt = 1/V_A { Q_{CA}P_{A*i*} - P_{A*i*} dV_A/dt - sum_{j=1}^{N_{seg}} [D_{L*i*}[P_{A*i*} - P_{b*i*}^(j)]ΔV_{PC}^j / V_{PC} } (30)

Here, P_{D*i*}, P_{C*i*}, and P_{A*i*} are partial pressures of gas species *i* (O₂ or CO₂) in the upper, middle, and small airways, respectively; P_{atm,*i*} is the partial pressure of the gas species *i* in the atmosphere; and V_{PC} is the blood volume contained in pulmonary capillary. N₂ partial pressure in the airways was obtained by subtracting the partial pressures of O₂, CO₂, and H₂O from the total airway pressure. N_{seg} is the number of capillary segments. In the gas exchange model, the lumped pulmonary capillary was divided into 35 segments, as in Liu et al. (18). P_{b*i*}^(j) represents the partial pressure of gas species *i* in the *j*th capillary segment, and ΔV_{PC}^j denotes the blood volume contained in the *j*th capillary segment.

The total flux rate (Φ_{tot}; in ml/s) of all gaseous species across the alveolar membrane can be expressed as follows

Phi_tot = sum_{i=1}^3 sum_{j=1}^{N_{seg}} [D_{L*i*}[P_{A*i*} - P_{b*i*}^(j)]ΔV_{PC}^j / V_{PC} (31)

Here, *i* = 1, 2, or 3 and represents the three gaseous species (O₂, CO₂, and N₂).

Species molar balance was employed to describe the dynamics of the species blood concentration in each segment. The corresponding equation for gas species *i* in the *j*th capillary segment is given by

partial C_{b*i*}^(j) / partial t = - partial v_{Z_b}^(j) C_{b*i*}^(j) / partial z + D_{L*i*}[P_{A*i*} - P_{b*i*}^(j)] / V_{PC} (32)

The formula of the lung diffusion capacity for each gaseous species was taken from Liu et al. (18) (with a change in units from ml STPD·min⁻¹·mmH₂O⁻¹ to ml STPD·s⁻¹·mmHg⁻¹). These formulas are as follows

D_{L,O₂} = sqrt(V_{PC} / V_{PC,max}) * (0.397 + 0.0085 P_{O₂} - 0.00013 P_{O₂}² + 5.1 * 10⁻⁷ P_{O₂}³) (33)

D_{L,CO₂} = sqrt(V_{PC} / V_{PC,max}) * 16.67 (34)

D_{L,N₂} = sqrt(V_{PC} / V_{PC,max}) * 0.25 (35)

where V_{PC,max} is the maximal blood volume in the pulmonary capillaries.

Cardiopulmonary Interactions

Any combined cardiovascular and pulmonary model must account for interactions that can occur between these systems. These interactions take a variety of forms and frequently are quite subtle. In general, to test for system interaction, a variable in one system is perturbed and the effects on both systems are assessed. We accomplished this by using only perturbations in pleural pressure (P_{PL}). The following sections provide simple examples of this coupled interaction.

How P_{PL} mediates cardiac and vascular mechanics. P_{PL} affects both intracardiac pressures and the pressures within the large intrathoracic vessels, but alveolar pressure has the greatest effect on pulmonary capillaries (18, 23). Consequently, in our model, the capillary transmural pressure is mediated by the alveolar pressure, whereas the pressures of the pulmonary arteries and veins are changed by P_{PL}.

How lung air volume changes lung perfusion. The pulmonary capillary bed forms an extensive network of vessels, which surround the alveolar region. During lung inflation, these vessels are stretched and constricted by the expanding alveolar volume. This increases capillary resistance and reduces blood flow, thus facilitating gas exchange. The relationship we used to describe the capillary resistance (R_{PC}) changes with alveolar volume (V_A) is as follows

R_{PC}(V_A) = R_{PC,0} * (V_A / V_{A,max})² (36)

Here, R_{PC,0} is a constant chosen to set the magnitude of capillary resistance and V_{A,max} represents the maximum alveolar volume.

COMPUTATIONAL ASPECTS

To summarize, we modified and combined previous cardiac and pulmonary models developed by our group to form a cardiopulmonary model of the normal human (Tables 8–10). The pulmonary models employed (2, 18) were originally developed as human models and were verified using data obtained from normal human subjects. However, the cardiovascular model used as a basis for designing our human circulatory model (25) was validated using data from the dog. To develop the human model, we first scaled up our canine model to

Table 8. Initial conditions used in the cardiovascular model

Compartments	Pressure, mmHg	Volume, ml	Flow, ml/s
<i>Heart</i>			
LA		90	
LV		130	
PCD		440	
RA		90	
RV		130	
SPT		10	
<i>Systemic Circulation</i>			
A _{oD}	12.5	200	70.6
A _{oP}	100.3	100	75.3
SA	110	225	
SA _D	50	174	
SC	18.6	300	
SV	6.4	3,000	
VC	6.3	240	
<i>Pulmonary Circulation</i>			
PA	15.6	75	
PA _D	16.3	35	67.5
PA _P	17.6	18	67.5
PC	14.2	110	
PV	12.3	200	

For abbreviations, see *Glossary* and text.

provide an initial model of the normal human cardiovascular system. This has been done by others (see, e.g., Ref. 17). Because human and canine blood pressures and blood velocities are similar, scaling factors are related closely to the ratios of blood volume. (Blood volume is directly related to body weight and body surface area.) In a second phase, we manually adjusted the parameters of the initial human circulatory model to yield a reasonable fit to typical human pressure data and hemodynamic indexes available in the literature.

First, we determined that the cardiac output of a 70-kg human is ~2.5 times that of a 25-kg dog. Because the mean systemic arterial pressures in the human and dog are similar, we calculated a set of human cardiovascular parameters by decreasing all the resis-

Table 9. Initial conditions used in the pulmonary model

Variables	Values
<i>Airway Mechanics</i>	
V _A , ml	2,200
V _C , ml	50
V _{CW} , ml	2,250
V _{VE} , ml	0
<i>Gas Exchange</i>	
P _{A,CO₂} , mmHg	42
P _{A,O₂} , mmHg	105
P _{b,CO₂} , mmHg	46
P _{b,O₂} , mmHg	40
P _{C,CO₂} , mmHg	30
P _{C,O₂} , mmHg	115
P _{D,CO₂} , mmHg	0.5
P _{D,O₂} , mmHg	150

For abbreviations, see *Glossary* and text.

Table 10. Initial conditions of the baroreflex model

Variables	Values
F _{con} , Hz	125
F _{Hr,S} , Hz	120
F _{Hr,V} , Hz	120
F _{vaso} , Hz	130
N ₁ , Hz	175
N ₂ , Hz/s	0

For abbreviations, see *Glossary* and text.

tive and inertial parameters of the canine model by 2.5 and by similarly increasing the compliant parameters. This scaling provided a reasonable initial representation of the human cardiovascular system, although additional adjustments were necessary for better regional representations of typical hemodynamic waveforms.

The representations used for certain elements of the canine and human circulatory models were different. Specifically, the linear representations of venous compliance in the canine model were replaced by nonlinear P-V relationships in the human model. Nonlinear active and passive P-V curves were also incorporated to describe arterial compliance.

The structure of the human circulatory model also differs in that several parallel circulation pathways were added. In the pulmonary circulation, the average pulmonary shunt flow is 2% of the pulmonary blood flow, whereas in the systemic circulation, the mean coronary and cerebral flows are set to 6% and 14%, respectively, of the cardiac output. The nominal distribution of blood volume in the pulmonary and systemic circulations are set at a level of 8.8% and 84%, respectively. The remaining 7.2% of the blood is contained in the heart. These figures agree with the results shown in Ref. 24 (p. 30 and 124).

We approximated the first-order spatial derivative in Eq. 32 using a four-point biased quadratic interpolation formula (31) and eliminated fictitious points at the entrance of the capillary bed using constant inlet conditions (i.e., partial pressures of 40 mmHg for O₂ and 46 mmHg for CO₂).

The P_{PL} data reported previously by Liu et al. (18) were used to directly drive the pulmonary model. Therefore, the respiratory frequency was determined directly from the experimental data. The model begins at end expiration, when there is no flow and air volume in the lung equals the functional residual capacity (FRC), which is set to the typical value of 2,200 ml.

The combined model has 77 nonlinear differential equations and 116 parameters associated with its component models. In all, 149 outputs were generated simultaneously. Table 11 shows the distribution of the state variables and model parameters in the combined cardiopulmonary model.

The model was programmed in C programming language and solved using the variable step-size Runge-Kutta-Merson algorithm, with a maximum time step size of 2×10^{-2} s and an error tolerance of 1×10^{-6} . On average, it takes 20 min of CPU time on a Pentium

Table 11. *Distribution of state variables, parameters, and outputs in the combined human cardiopulmonary model*

	Number of State Variables	Number of Parameters	Number of Outputs
Cardiovascular system	32	52	76
Airway mechanics	4	10	7
Gas exchange	36	24	50
Baroreflex control	5	30	16
Total	77	116	149

II 333-MHz machine to simulate 35 s of cardiopulmonary events.

Simulation Results

Hemodynamics. Figure 6 compares a model-generated and human systemic pressure waveform (Fig. 22.15 in Ref. 20). The left ventricular end-systolic pressure is 125 mmHg and the systolic duration is 0.3 s, or about one-third of the cardiac cycle (0.8 s). The aortic root pressure ranges from 80 to 120 mmHg. The dirotic notch can be clearly seen in both the simulation and the data.

Figure 7 compares experimental data to the model-generated left ventricular volume and aortic and pulmonary arterial flow waveforms (Fig. 6-1 in Ref. 24). The left ventricular volume ranged from 150 ml [end-diastolic volume (V_{ED})] to 70 ml [end-systolic volume (V_{ES})], giving a stroke volume of 80 ml and an ejection fraction of 80/150, or 0.533. The volume added as the result of atrial systole (ΔV) was 30 ml, ~20% of the V_{ED} . The peak aortic flow rate was 750 ml/s and the peak pulmonary arterial flow rate was 400–500 ml/s. The aortic flow rate has a higher peak value and shorter time span compared with the pulmonary flow rate because of the stronger contractile force and higher afterload of the left ventricle. Numerical integration of the aortic and pulmonic flow waveforms over one cycle showed that the mean values of the area enclosed by the two waveforms were the same, although during individual cardiac cycles they may be different from each other due to variations of intrathoracic pressure.

Table 12 compares indexes of the model-predicted and measured data. Our model predicts that at peak inspiration, the stroke volume of the left heart decreases, whereas the stroke volume of the right heart increases. At peak expiration, the opposite occurs. These changes agreed well with measured data (4, 9, 13, 26, 28). Our model helps explain the mechanism underlying this physiological relationship.

Right and left ventricular volumes respond to P_{PL} because of both direct and series ventricular interaction. When P_{PL} are negative (e.g., with inspiration), an increase in venous return augments right ventricular filling and stroke volume. The increased right ventricular filling causes the septum to encroach upon the left ventricle, because the pericardium limits total cardiac volume. As a result, left ventricular stroke volume is reduced. Simulations that ignore this ventricular interaction (rigid septum) underestimate the percent fall in left ventricular stroke volume occurring during inspiration (2.5% vs. 5% with ventricular interaction). Without pericardial constraint, there is little respiratory variation in left ventricular stroke volume (1%).

Expiration causes a volume shift from the pulmonary to the systemic circulation. The blood pooling in the systemic vascular bed then increases left ventricular afterload with the next inspiration. Simulations show that both the end-systolic transmural pressure and volume of the left ventricle are highest at early inspiration, consistent with increased afterload (27, 30, 32). During inspiration, both decreased filling and increased afterload decrease left ventricular stroke volume. The same mechanism explains why the left and right ventricles respond differently to elevated P_{PL} during expiration.

Airway Mechanics and Gas Exchange

Figure 8 depicts the airway pressures and lung volumes predicted by our model. During inspiration, sub-atmospheric P_{PL} is transmitted to the alveoli, facilitating air flow into the lungs. As this occurs, lung elastic recoil increases and the alveolar and atmospheric pressures equalize, marking the end of inspiration and the start of expiration. During expiration, the less negative P_{PL} and the resulting changes in lung elastic recoil cause positive alveolar pressure, pushing air from the

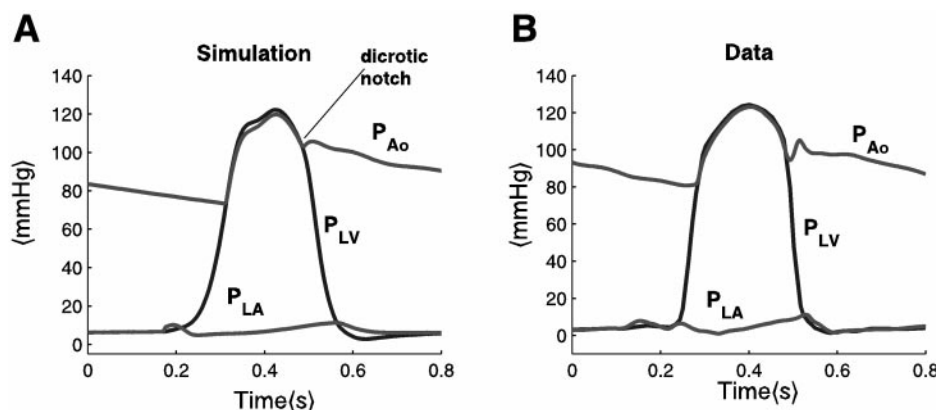


Fig. 6. Model-predicted systemic pressure waveforms (A) compared with the textbook figure [McClintic (20); B] showing left ventricular pressure (P_{LV}), aortic root pressure (P_{Ao}), and left atrial pressure (P_{LA}).

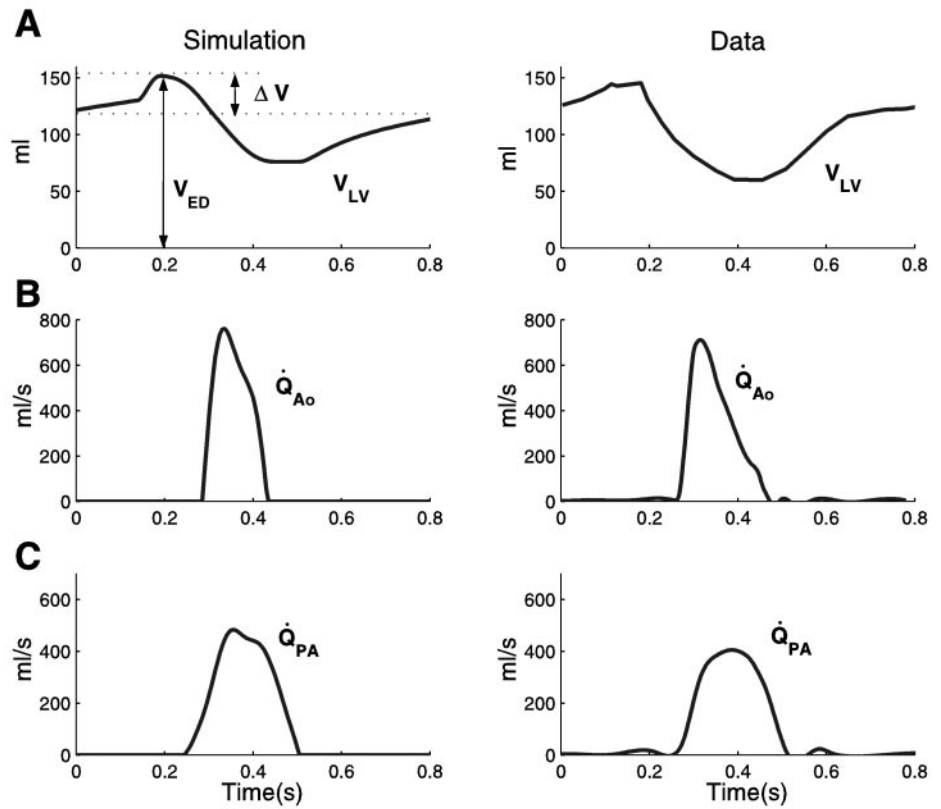


Fig. 7. Model-predicted volumes and flows (left) compared with reported experiment data [Mountcastle (24); right]. A: left ventricular volume (V_{LV}); B: aortic flow (\dot{Q}_{Ao}); C: pulmonary arterial flow (\dot{Q}_{PA}). For abbreviations, see text.

lungs. The inspiratory and expiratory changes in lung volume are depicted in Fig. 8B. Here, total lung volume is the sum of the air volumes contained in the alveoli, collapsible airways, and dead space. The model predicts an average tidal volume of 500 ml and a functional residual capacity (FRC) of 2.2 l, which agreed with measured values.

Inspiration fills the alveoli with O_2 -enriched air, whereas expiration removes CO_2 . Figure 9 depicts the model-generated variation in airway gas composition in terms of changes in the partial pressures of O_2 and CO_2 (P_{O_2} and P_{CO_2} , respectively). Alveolar PCO_2 and PO_2 are relatively constant. Alveolar PO_2 varies from 95 to 105 mmHg, and alveolar PCO_2 varies from 35 to 40 mmHg. With inspiration, PO_2 in the upper airways (dead space) rises sharply, whereas PCO_2 drops

sharply. However, not all inhaled air enters the alveoli, and inhaled and residual air mix, making variations in alveolar PO_2 and PCO_2 much smaller than those in the dead space. Expiration lowers the PO_2 and raises the PCO_2 in the dead space, whereas gases continuously diffuse across the alveolar-capillary membrane. Conse-

Table 12. Comparison of hemodynamic indexes drawn from model-predicted and measured data

Hemodynamic Variables	Model-Predicted Data	Measured Data
Aortic root pressure, mmHg	80–125	80–120
Ejection fraction, %	53.3	56.7
LV end-diastolic volume, ml	150	150
LV end-systolic pressure, mmHg	125	120
LV end-systolic volume, ml	70	65
Peak aortic flow, ml/s	780	720
Peak pulmonary arterial flow, ml/s	500	450

Measured data values are from McClintic (20) and Mountcastle (24).

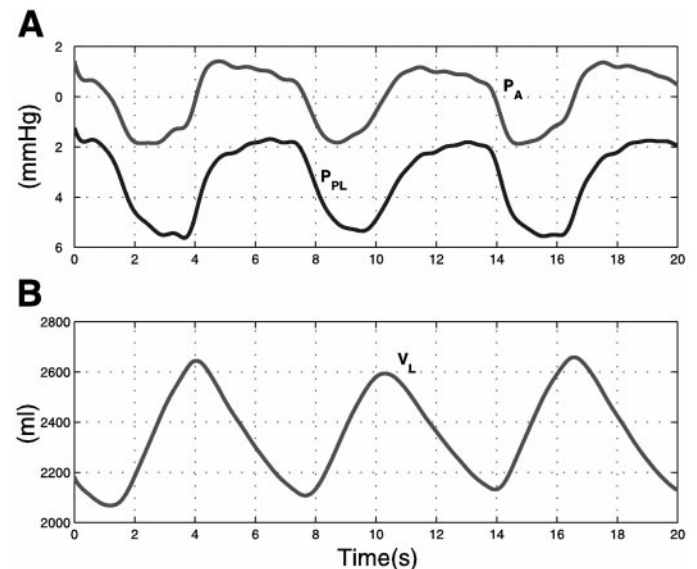


Fig. 8. Model-predicted airway pressures and lung volume in normal breathing. A: model-generated alveolar pressure (P_A). P_{PL} , experimental data of the pleural pressure. B: lung volume (V_L). The lung volume includes air volumes in the alveolar region, collapsible airways, and dead space.

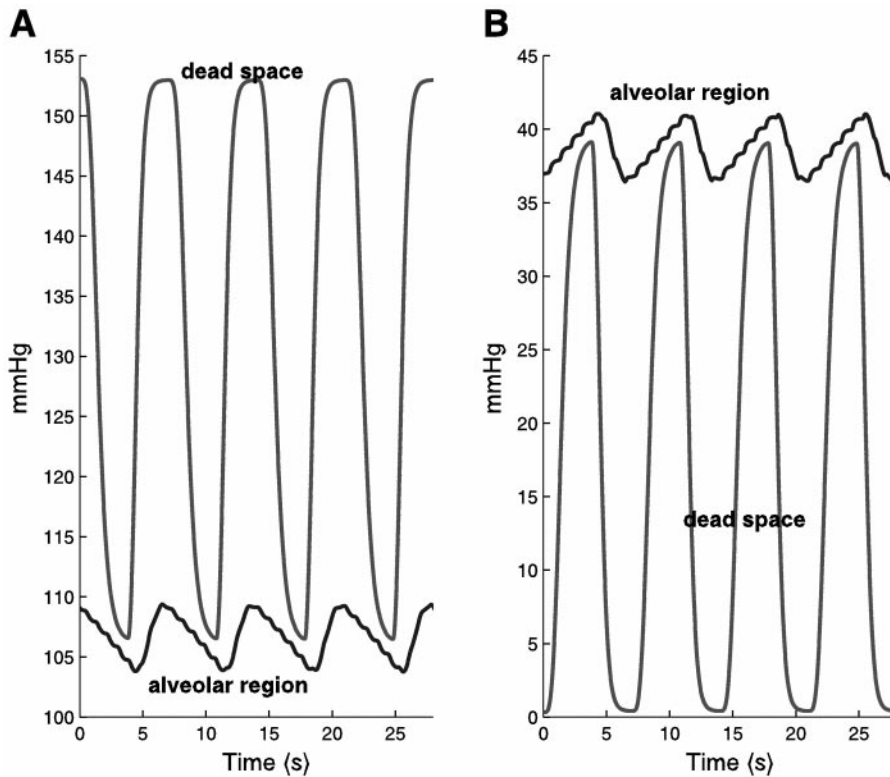


Fig. 9. Variations of airway gaseous partial pressure during normal breathing in the simulation. *A*: PO_2 variations in the dead space and alveolar regions. *B*: PCO_2 variations in the dead space and alveolar regions.

quently, alveolar PO_2 decreases and alveolar PCO_2 increases.

Alveolar capillary gas exchange. Figure 10 depicts the flux of O_2 and CO_2 at the alveolar-capillary membrane, which is modeled as 35 contiguous segments. For each segment, there is a gaseous flux waveform that pulsates with capillary blood flow. Most gaseous diffusion occurs at the initial capillary segments but

later diminishes when blood and alveolar gas content has equilibrated. Thus the flux rates decrease exponentially from the first (entrance) to the last segment (exit). We tested our model against the known changes that occur during the FVC and Valsalva maneuvers.

Forced Vital Capacity Maneuver

The FVC maneuver is a commonly used pulmonary function test. The subject fully exhales and then inhales to total lung capacity (TLC) without pausing. Immediately, the subject exhales as rapidly as possible, until airflow is no longer detected at the mouth. We applied the measured FVC P_{PL} data reported in Ref. 18 to our model.

Figure 11 compares the model predictions to data measured from a human. During the rapid inspiration phase, lung volume increased to full capacity (Fig. 11A) and P_{PL} decreased (Fig. 11B). At the beginning of forced expiration, P_{PL} increases sharply, and lung volume decreased until it reached residual volume. The predicted and measured data correlated nicely.

During the FVC maneuver, the expired PO_2 decreased constantly and reached a minimum value of 118 mmHg. In contrast, PCO_2 increased steadily until its maximum value of 38 mmHg. Figure 12 compares the predicted temporal profile of PO_2 and PCO_2 in expired air with data from Liu et al. (18). Again, the model prediction agreed well with the measured data.

Hemodynamic changes are seldom recorded during the FVC maneuver, but our model can predict them. Figure 13 shows the predicted change in left and right heart stroke volumes. As in normal respiration, the left

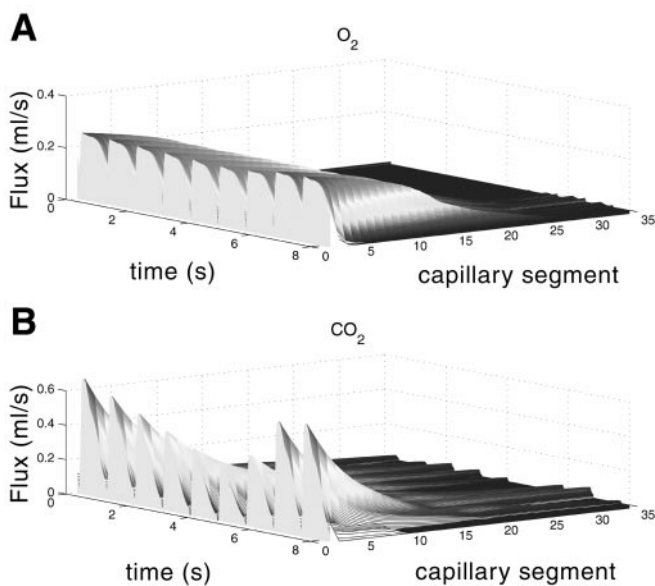


Fig. 10. Three-dimensional representations of the regional gaseous flux calculated at each of the 35 capillary segments. *A*: O_2 gas flux; *B*: CO_2 gas flux.

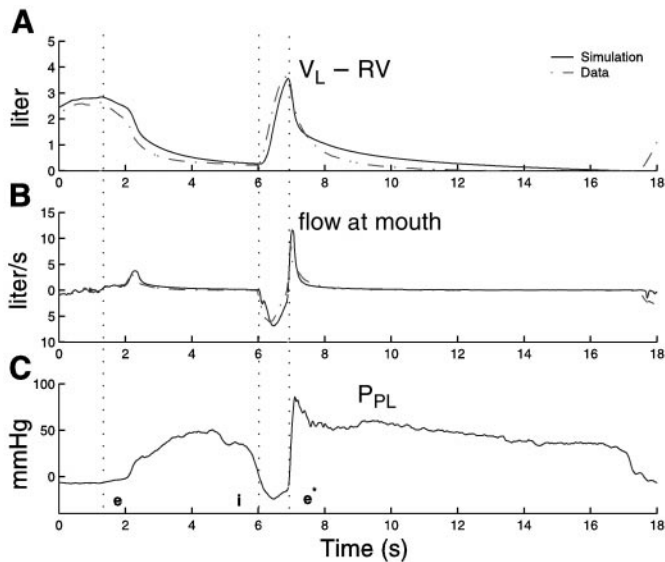


Fig. 11. Model predictions of lung volume variations and flow at the mouth (solid lines) compared with experimental data (dashed lines) from Liu et al. (18). The dotted vertical lines show the first expiration (e), inspiration (i), and second expiration (e*). A: lung volume (V_L) variations from residual volume. B: flow at the mouth. C: measured P_{PL} data.

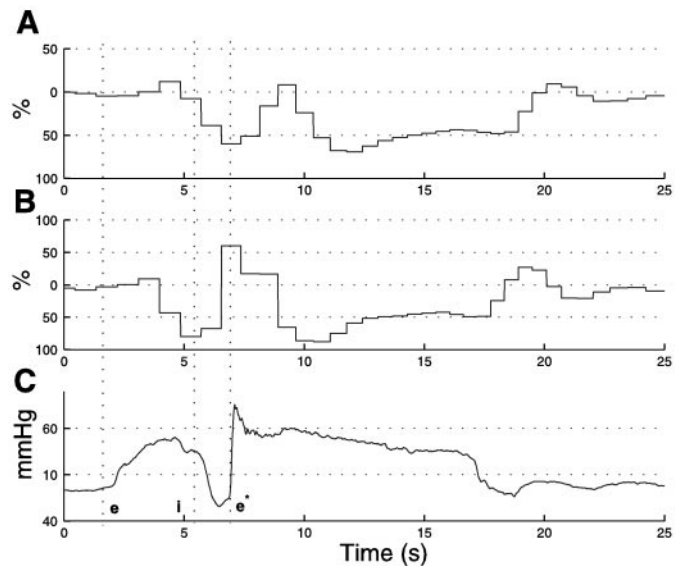


Fig. 13. Model-predicted percent changes in left (A) and right ventricular stroke volumes (B) during the FVC maneuver. C: P_{PL} data from Liu et al. (18). The dotted vertical lines show the first expiration (e), inspiration (i), and second expiration (e*).

and right ventricles showed opposite responses during inspiration and the early part of the forced expiration. However, after a few beats into the prolonged second phase of forced expiration, the stroke volumes of both ventricles decreased quickly and then returned to baseline after an overshoot (Fig. 13). Stroke volume decreases because elevated P_{PL} decreases venous return. The recovery and the overshoot may be caused by neural factors (discussed below).

Figure 14 demonstrates a similar recovery and overshoot in the systemic arterial pressure waveform (A) and the temporal variations in heart rate (B), vagal discharge (C), and sympathetic discharge (D). Heart rate increases slowly during the maneuver. Vagal efferent activity slows, and a burst of sympathetic activity occurs later. These findings are consistent with the faster and slower activity of the vagal and sympathetic pathways, respectively. The decreasing vagal and increasing sympathetic outputs correlated with the ob-

served increases in heart rate, myocardial contractility, and vasomotor tone and explained the partial recovery of arterial blood pressure that occurs during and shortly after the maneuver.

Valsalva Maneuver

During the Valsalva maneuver, the subject forcefully exhales against a closed glottis (or nose and mouth). The maneuver markedly elevates intrathoracic pressure and affects venous return, myocardial contractility, vasomotor tone, and baroreflex heart rate control. It is a widely used test of baroreceptor reflexes (6).

The hemodynamic response to the Valsalva maneuver has four distinct phases: *phase 1* (an initial increase in arterial pressure), *phase 2* (a rapid fall in arterial pressure, followed by a partial recovery and tachycardia), *phase 3* (a reduction in arterial pressure upon the sudden termination of breath holding, accompanied by a continued tachycardia), and *phase 4* (an

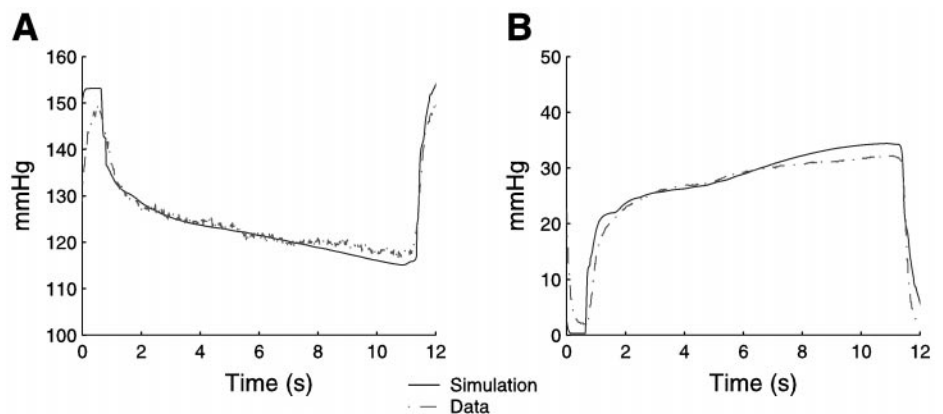


Fig. 12. Model-predicted PO_2 and PCO_2 (A) in the expired air at the mouth (solid lines) during the forced expiration in the forced vital capacity (FVC) maneuver compared with experimental recordings (dashed lines) from Liu et al. (18).

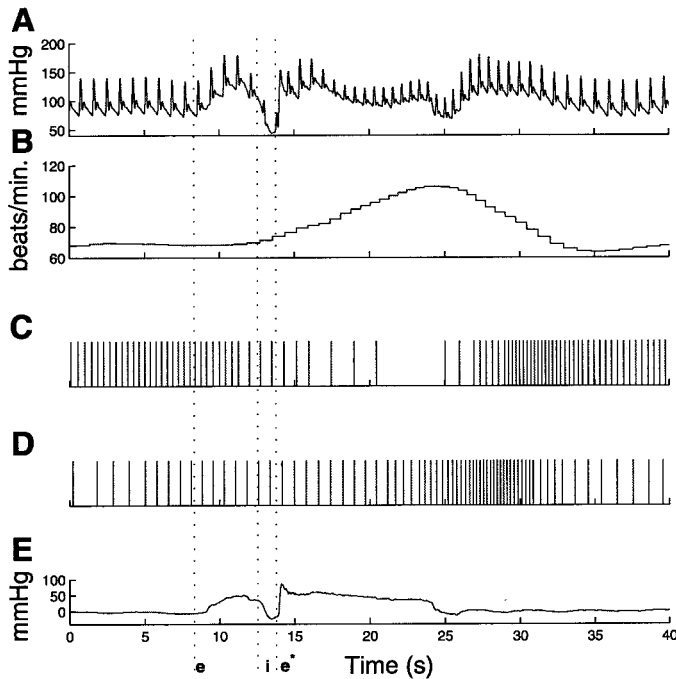


Fig. 14. Model-predicted variables during the FVC maneuver. *A*: systemic arterial pressure (P_{SA}); *B*: heart rate; *C*: vagal efferent discharge; *D*: sympathetic efferent discharge; *E*: P_{PL} data from Liu et al. (18). The dotted vertical lines show the first expiration (e), inspiration (i), and second expiration (e^*).

overshoot in arterial pressure accompanied by a slowing of heart rate).

In our model, we simulated the Valsalva maneuver by elevating P_{PL} to a higher value for 15 s, starting at the end of both inspiration and diastole. P_{PL} of 10, 20, 30, and 40 mmHg were used in the simulation to represent different levels of expiratory effort. Airflow in the airways was set to zero during the maneuver to simulate the closed glottis.

Figure 15 compares the model-generated changes in arterial pressure and heart rate when P_{PL} is 40 mmHg during the Valsalva maneuver with the experimental data from Bannister (33). The predicted increase in arterial pressure during *phase 1* (~120% of baseline), recovery of the arterial pressure during *phase 2*, and overshoot during *phase 4* (20% above baseline) all fitted well with the measured data, as did the predicted heart rate changes. Heart rate peaked at 110 beats/min and dropped to 62 beats/min after the maneuver. However, the predicted heart rate changes before and after the maneuver were much smoother than the measured data. This may be because an idealized square P_{PL} waveform was used in the Valsalva maneuver simulation. In reality, P_{PL} recordings show fluctuations before and after the maneuver.

Figure 16 shows heart rate, cardiac output, and mean arterial pressure as a function of P_{PL} during the Valsalva maneuver. Experimental data from Korner et al. (14) were superimposed on the plot. Both heart rate and mean arterial pressure increased nearly linearly as P_{PL} increased. Because of reduced venous return, cardiac output declined with the increase in P_{PL} .

Table 13 shows that a variety of calculated hemodynamic indices evaluated from the model predictions during the Valsalva maneuver agreed well with those obtained from humans [Fox et al. (8)].

Baroreflex control during the Valsalva maneuver. The Valsalva maneuver changes autonomic tone, central nervous system activity, arterial blood pressure, and heart rate. Figure 17 illustrates how heart rate, myocardial contractility, and vasomotor tone responded to baroreflex control during each phase of the Valsalva maneuver.

Phase 1 elevation of arterial pressure occurs without baroreflex control, suggesting that the elevation is due only to the mechanical forces of increased intrathoracic pressure (6), which compresses the heart chambers and augments output to the periphery.

Phase 1 lasts about one to two heartbeats. As venous return is reduced by the elevated intrathoracic pressure, diastolic filling and stroke volume decrease. Therefore, in *phase 2*, blood pressure decreases and heart rate increases, with baroreflexes helping maintain arterial pressure and cardiac output. Simulations demonstrate the importance of baroreflex control.

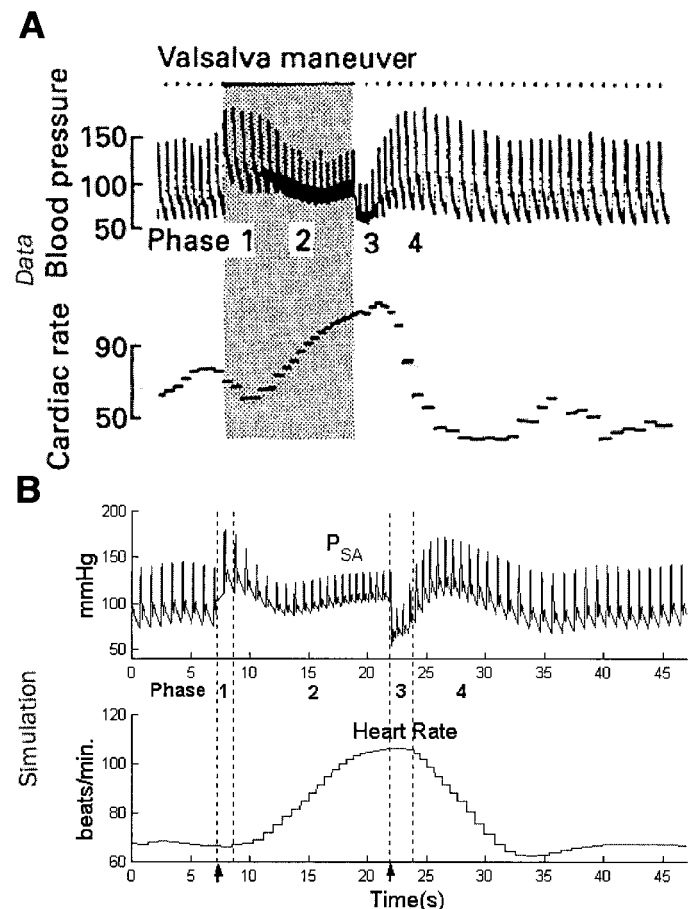


Fig. 15. Comparison of experimental data [Bannister (33); *A*] with model-based predictions (*B*) of the changes in P_{SA} (top) and heart rate (bottom) during the Valsalva maneuver. The arrows in *B*, bottom, denote the beginning and end of the maneuver. The four distinct phases of the Valsalva maneuver are indicated by the vertical dashed lines and numbers.

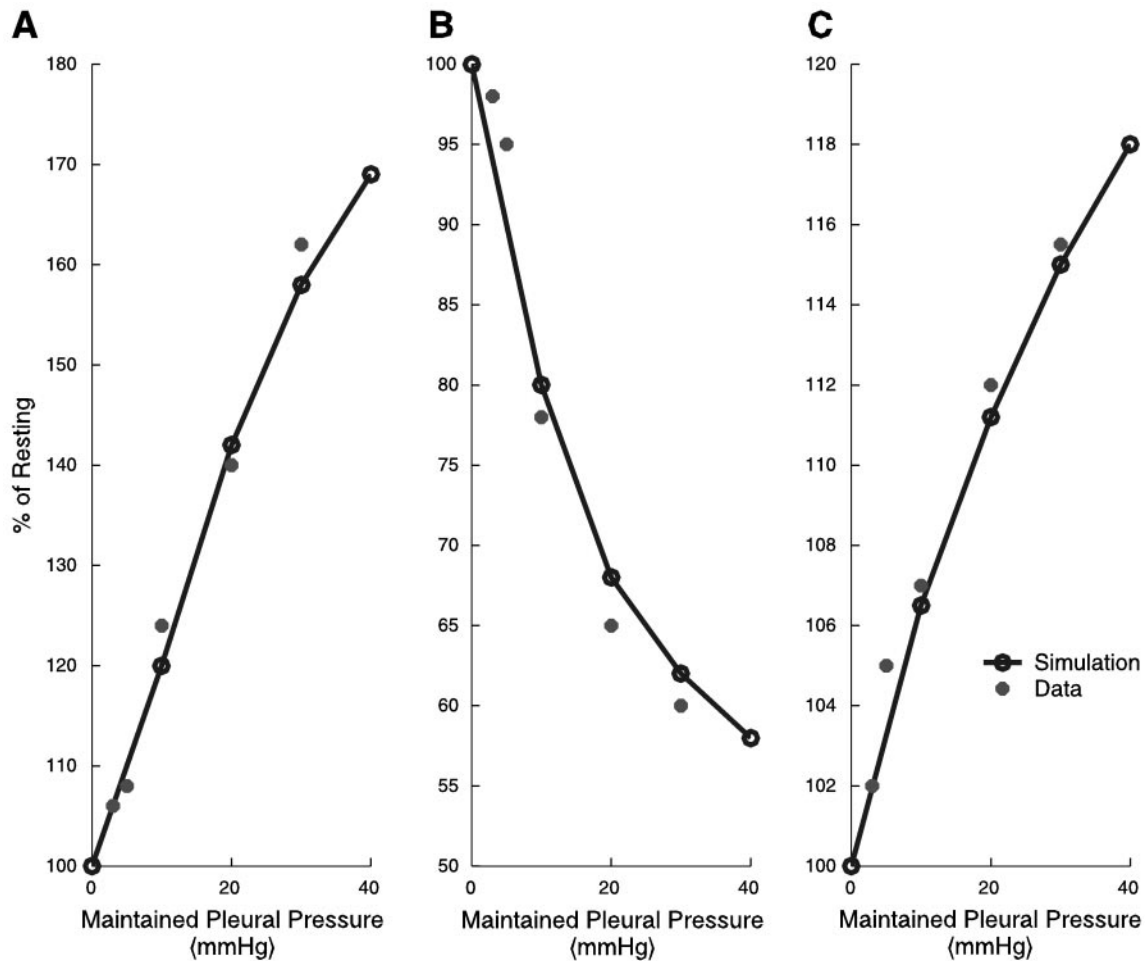


Fig. 16. Relationships between P_{PL} and heart rate (A), cardiac output (B), and mean arterial pressure (C) during the Valsalva maneuver. [Data source: Korner et al. (14).]

When baroreflex control was abolished (Fig. 17A), arterial pressure dropped during this phase. When the sympathetic vasomotor tone was added (Fig. 17B), the reduction in arterial pressure leveled off after five to six beats, and arterial pressure stabilized. When myocardial contractility was added (Fig. 17C), a slow and gradual recovery of arterial pressure toward baseline occurred after six beats. The delay corresponded to the late increase in sympathetic efferent traffic (Fig. 18C), which constricts arterial resistive vessels and augments myocardial contractility. When baroreflex control of heart rate was included (Fig. 17D), heart rate increased. These simulations demonstrate the importance of baroreflex control during *phase 2* of the Valsalva maneuver.

During *phase 3*, the model predicts a fall in arterial pressure without baroreflex input (Fig. 17A). The decrease in intrathoracic pressure decreased intracardiac pressure and stroke volume. Heart rates remained high due to the increased sympathetic tone (Fig. 18C).

During *phase 4*, venous return became normal. However, the delayed sympathetic response maintained the heightened myocardial contractility, tachycardia, and vasoconstriction. With no baroreflex control (Fig. 17A),

arterial pressure slowly returned to baseline. With vasoconstriction (Fig. 17B), there was a small overshoot in arterial pressure even though arterial pressure returned to normal. This overshoot was more prominent (120% of the baseline level) when baroreflex control of myocardial contractility was added (Fig. 17C). Adding heart rate control (Fig. 17D) augmented this overshoot to a lesser degree.

The variations of vagal and sympathetic discharge frequencies during the maneuver are shown in Fig. 18. During *phase 2*, vagal discharges diminished and sympathetic discharges increased. The increase in sympathetic tone occurred after vagal tone decreased. Immediately after the release of the strain, vagal discharge frequency quickly returned toward control, whereas the elevated sympathetic tone continued into the late part of *phase 4*.

Figure 19 summarizes how the individual baroreflex pathways maintain arterial pressure. In *phase 2*, vasoconstriction prevented arterial pressure from dropping at a constant rate, whereas increased myocardial contractility and tachycardia helped restore arterial pressure and cardiac output. Continued increases in myocardial contractility and vasomotor control contrib-

Table 13. Summary of model-predicted changes in hemodynamic indexes during the Valsalva maneuver

	Model-Predicted Data	Measured Data
<i>Cardiac Output</i>		
Control, l/min	5.0	4.2
Phase 1, %Control	96	97
Phase 2, %Control	45	39
Phase 3, %Control	55	36
Phase 4, %Control	120	107
<i>Heart Rate, beats/min</i>		
Control	68	72
Phase 1	66	65
Phase 2	105	97
Phase 3	107	105
Phase 4	62	57
<i>Pulmonary Arterial Pressure, mmHg</i>		
Control	30/5	23/12
Phase 1	65/48	53/46
Phase 2	55/43	50/44
Phase 3	19/2	22/11
Phase 4	35/8	28/15
<i>Systemic Arterial Pressure, mmHg</i>		
Control	140/80	143/88
Phase 1	180/120	161/102
Phase 2	120/90	108/83
Phase 3	90/60	97/73
Phase 4	170/110	178/100

Index values were compared with measured data values in each of the 4 stages (phases 1–4). Measured data values are from Fox et al. (8).

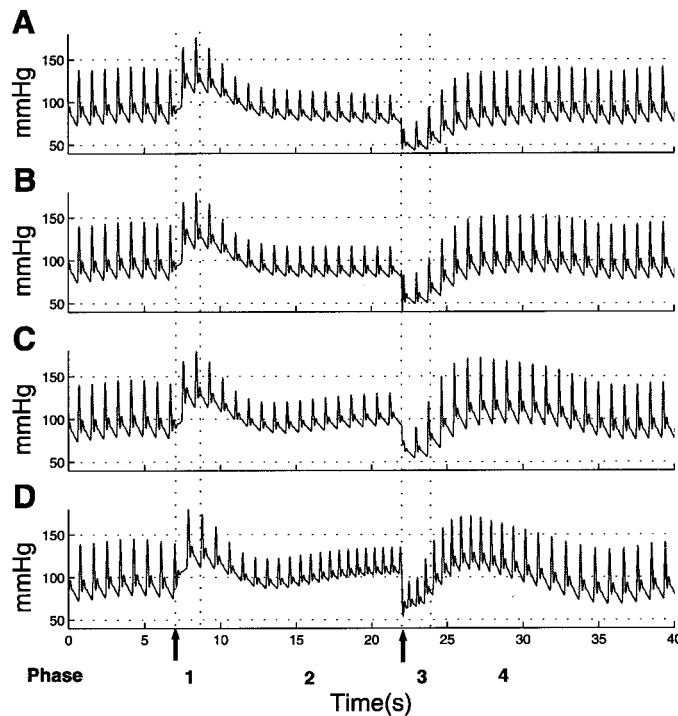


Fig. 17. Model-generated arterial pressure waveforms during the Valsalva maneuver under four baroreflex control conditions. A: no baroreflex control present; B: only the vasomotor tone control; C: vasomotor tone + myocardial contractility control; D: all 3 control components (vasomotor tone, myocardial contractility, and heart rate). The arrows indicate the start and the end of the maneuver.

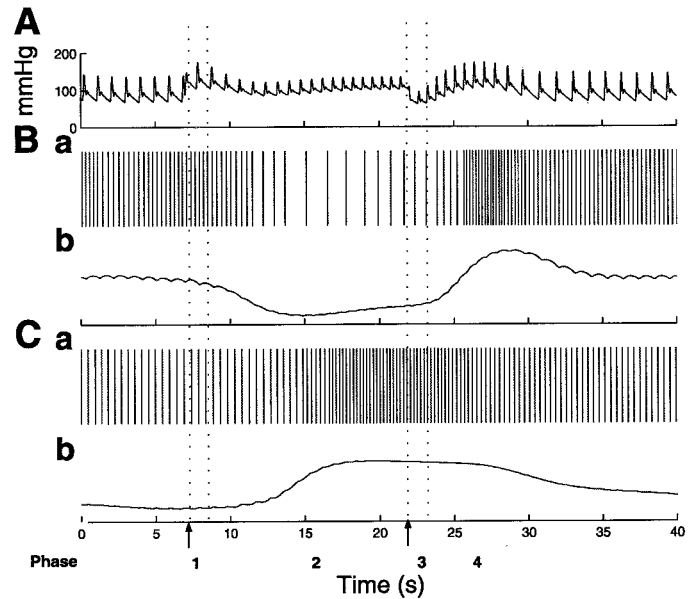


Fig. 18. Model-generated sympathetic and parasympathetic (vagal) efferent bursts during the Valsalva maneuver. A: P_{SA} response. B: vagal discharge frequency [showing both the spike representation (a) and the relative changes of the frequency value (F_{vagus}); b)]. C: sympathetic discharge frequency [showing both the spike representation (a) and the relative changes of the frequency value (F_{symp}); b)]. The arrows indicate the start and the end of the maneuver.

uted strongly to the overshoot of arterial pressure in phase 4.

DISCUSSION

We presented a mathematical model of the human cardiopulmonary system that combines several component models previously developed by our group. Physiological data predicted by this combined model agreed well with data taken from resting and normal subjects in the supine position. The model was further validated by accurately predicting the sudden and large physio-

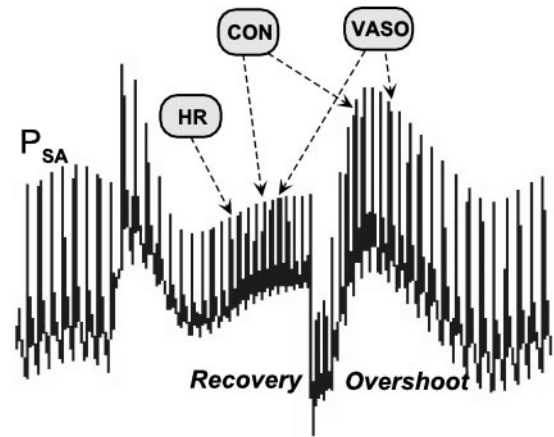


Fig. 19. Schematic representation of the contribution of the individual baroreflex pathway to the P_{SA} response during the Valsalva maneuver. HR, heart rate; CON, myocardial contractility; VASO, vasomotor tone.

logical changes that occurred during the FVC test and all four stages of the Valsalva maneuver.

Although the Valsalva maneuver is well understood, it remains a relatively complicated physiological response, with mechanical and autonomic components that are difficult to separate when used clinically. This limits what information might be obtained from a test that otherwise is very helpful, easy to perform, and commonly used to assess patients with a wide variety of cardiovascular disorders. Because our cardiopulmonary system can mimic a combined response from separate pulmonary, circulatory, and neural components, actual (clinical) responses to the Valsalva maneuver might be analyzed in terms of these components (see Fig. 18 and its accompanying discussion), and a specific physiological defect may be more easily identified. It is also possible that variations between or within groups may be more amenable to statistical analysis, because of the purely quantitative nature of the model. Good statistical backing would certainly improve the meaning and significance of future studies using the Valsalva maneuver.

The utility of our cardiopulmonary model should not be limited to the Valsalva maneuver, however. With further modification and extension, it might help diagnose or analyze other normal or disordered physiological responses, such as orthostatic hypotension, and could characterize disease states such as atherosclerosis, valvular stenosis, and the pulmonary effects of congestive heart failure and the adult respiratory distress syndrome. It could also be helpful in assessing the prognosis of patients with congestive heart failure and/or coronary artery disease, because in these patients both autonomic and mechanical dysfunction are major determinants of premature death.

Model Limitations

All models have limitations, and ours is no exception. The following are a discussion of the limitations of our model:

We employed a circulatory model of intermediate complexity for use in the larger cardiopulmonary model. It mimics the hemodynamics of the circulation quite well. The objectives of the study are general, however, and if questions such as flow in a particular circulation or pulse wave propagation were asked of this model, its foundational assumptions would be too crude to provide adequate predictions (e.g., wave propagation delay is approximated by a phase shift). In addition, as a supine model, it cannot simulate the hemodynamic responses related to changes in body position or gravitational forces, e.g., when subjects stand up from the supine position or enter different gravitational environments as in space flight. To address such problems, additional bandwidth (structural changes) would have to be provided in the form of the adoption of a more distributed model or certain nonlinear elements would have to be included. This, however, is the subject matter of another study.

Ventricular elastance is defined as the instantaneous transmural pressure-to-ventricular volume ratio. At each point in time, it represents a linear relationship between pressure and volume. Therefore, it provides only an approximation to the curvilinear Frank-Starling relationship (5). This approximation works well around the operational point of the human heart, but with large increase in volume, it would overestimate the pressure developed by the ventricle. To represent the Frank-Starling mechanism more faithfully, the expression for elastance should be modified and made a function of both end-diastolic volume (V_{ED}) and time, as in Ref. 10a.

The lung was characterized as a single compartment, and homogeneous ventilation was assumed. This is unsuitable when the lungs have regional disease. A multiple-compartment model would be required in that case.

The neural control scheme currently employed in the cardiopulmonary model includes only the baroreceptor-mediated control of heart rate, myocardial contractility, and vasomotor tone. It does not contain an explicit description of the splanchnic circulation, which in humans has a venous bed richly innervated by adrenergic nerve fibers. To develop quantitative descriptions of venoconstriction in humans, more data are needed. Therefore, we neglected venoconstriction as an important baroreceptor-mediated effect in the Valsalva maneuver. Other important factors, such as the cardiopulmonary baroreceptors, hormonal effects, central and peripheral chemoreceptor-mediated ventilation, and autoregulation of special circulations, are not considered in the current model. These factors can also exert important effects on the heart, circulatory hemodynamics, pulmonary mechanics, and ventilatory control.

The model characterizes gas exchange only at the alveolar-capillary membrane. However, gaseous partial pressures in pulmonary arterial blood at the inlet to this membrane are not constant, because gas exchange occurs at other tissue sites in the body. Modifying the model to characterize this additional tissue gas exchange would affect the gaseous content of the pulmonary arterial blood presented to the alveolar membrane.

Finally, the model must be refined by comparing its predictions with clinical data obtained prospectively.

The authors acknowledge the helpful comments of Drs. Dirar Khoury and Sherif Nagueh of Baylor College of Medicine in the preparation of the manuscript.

This work was supported by the Bioengineering Center, University of Texas Medical Branch, Galveston, TX.

REFERENCES

1. **Amoore JN and Santamore WP.** Model studies of the contribution of ventricular interdependence to the transient changes in ventricular function with respiratory efforts. *Cardiovasc Res* 23: 683–694, 1989.
2. **Athanasiaides A, Ghorbel F, Clark JW, Niranjana SC, Olansen JB, Zwischenberger JB, and Bidani A.** Energy analysis of a nonlinear model of the normal human lung. *J Biol Sys* 8: 115–139, 2000.



3. **Beyar R and Goldstein Y.** Model studies of the effects of the thoracic pressure on the circulation. *Ann Biomed Eng* 15: 373–383, 1987.
4. **Brinker JA, Weiss JL, Lappe DL, Rabson JL, Sumner WR, Permutt S, and Weisfeldt ML.** Leftward septal displacement during right ventricular loading in man. *Circulation* 61: 626–633, 1980.
5. **Chung D, Niranjana S, Clark JW, Bidani A, Johnston WE, Zwischenberger JB, and Traber DL.** A dynamic model of ventricular interaction and pericardial influence. *Am J Physiol Heart Circ Physiol* 272: H2942–H2962, 1997.
6. **Eckberg DL and Sleight P.** *Human Baroreflexes in Health and Disease*. Oxford, UK: Clarendon, 1992.
7. **Elad D and Kamm R.** Parametric evaluation of forced expiration using a numerical model. *J Biol Mech Eng* 111: 192–199, 1989.
8. **Fox IJ, Crowley WP, Grace JB, and Wood EH.** Effect of the Valsalva maneuver on blood flow in the thoracic aorta in man. *J Appl Physiol* 21: 1553–1560, 1966.
9. **Gabe IT, Gault JH, Ross J Jr, Mason DT, Mills CJ, Schillingford JP, and Braunwald E.** Measurement of instantaneous blood flow velocity and pressure in conscious man with a catheter-tip velocity probe. *Circulation* 40: 603–614, 1969.
10. **Gore RW and Davis MJ.** Mechanics of smooth muscle in isolated single microvessels. *Ann Biomed Eng* 12: 511–520, 1984.
- 10a. **Greene ME, Clark JW Jr, Mohr DN, and Bourland HM.** A mathematical model of left-ventricular function. *Med Biol Eng Comput* 1973, 126–134.
11. **Hainsworth R.** The physiological approach to cardiovascular reflexes. *Clin Sci* 91, Suppl: 43–49, 1996.
12. **Hardy HH, Collins RE, and Calvert RE.** A digital computer model of the human circulatory model. *Med Biol Eng Comput* 20: 550–564, 1982.
13. **Karam M, Wise RA, Natarajan TK, Permutt S, and Wagner NH.** Mechanism of decreased left ventricular stroke volume during inspiration in man. *Circulation* 69: 866–873, 1984.
14. **Korner PI, Tonkin AM, and Uther JB.** Reflex and mechanical circulatory effects of graded Valsalva maneuvers in normal man. *J Appl Physiol* 40: 434–440, 1976.
15. **Kresch E.** *Design of a non-linear electrical model for veins* (PhD thesis). Philadelphia, PA: University of Pennsylvania, 1968.
16. **Lambert RK, Wilson TA, Hyatt RE, and Rodarte JR.** A computational model for expiratory flows. *J Appl Physiol* 52: 44–56, 1982.
17. **Li JK-J.** *Comparative Cardiovascular Dynamics of Mammals*. Boca Raton, FL: CRC, 1996.
18. **Liu CH, Niranjana SC, Clark JW, San KY, Zwischenberger JB, and Bidani A.** Airway mechanics, gas exchange, and blood flow in a nonlinear model of the normal human lung. *J Appl Physiol* 84: 1447–1469, 1998.
19. **Lutchen KR, Suki B, Zhang Q, Petak F, Daroczy B, and Hantos Z.** Airway and tissue mechanics during physiological breathing and bronchoconstriction in dogs. *J Appl Physiol* 77: 373–385, 1994.
20. **McClintic JR.** *Basic Anatomy and Physiology of the Human Body* (2nd ed.). New York: Wiley, 1975.
22. **Melchior FM, Srinivasan RS, and Charles JB.** Mathematical modeling of human cardiopulmonary system for simulation of orthostatic response. *Am J Physiol Heart Circ Physiol* 262: H1920–H1933, 1992.
23. **Milnor WR.** Pulmonary hemodynamics. In: *Cardiovascular Fluid Dynamics*, edited by Bergel DH. New York: Academic, 1972, vol. 2, p. 299–340.
24. **Mountcastle VB, ed.** *Medical Physiology*. St. Louis, MO: Mosby, 1968, vol. 1.
25. **Olansen JB, Clark JW, Khoury D, Ghorbel FH, and Bidani A.** A closed-loop model of the canine cardiovascular system that includes ventricular interaction. *Comput Biomed Res* 33: 260–295, 2000.
26. **Olsen CO, Tyson GS, Maier GW, Davis JW, and Rankin JS.** Diminished stroke volume during inspiration: a reverse thoracic pump. *Circulation* 72: 668–679, 1985.
27. **Parsons GH and Green JF.** Mechanisms of pulses paradoxus in upper airway obstruction. *J Appl Physiol* 45: 598–603, 1978.
28. **Ruskin J, Bache RJ, Rembert JC, and Greenfield J.** Pressure-flow studies in man: effect of respiration on left ventricular stroke volume. *Circulation* 48: 79–85, 1973.
29. **Sato T, Kawada T, Inagaki M, Shishido T, Yakaki H, Sugimachi M, and Sunagawa K.** New analytic framework for understanding sympathetic baroreflex control of arterial pressure. *Am J Physiol Heart Circ Physiol* 276: H2251–H2261, 1999.
30. **Scharf SM, Brown R, Saunders N, and Greens LH.** Effect of normal and loaded spontaneous inspiration on cardiovascular function. *J Appl Physiol* 47: 582–590, 1979.
31. **Schiesser WE.** *Computational Mathematics in Engineering and Applied Science: ODEs, DAEs, PDEs*. Boca Raton, FL: CRC, 1994.
32. **Shuler RH, Ensor C, Ginning RE, Moss WG, and Johnson V.** The differential effects of respiration on the left and right ventricles. *Am J Physiol* 137: 620–627, 1942.
33. **Bannister R.** *Arterial Blood Pressure and Hypertension*, edited by Sleight P. Oxford, UK: Oxford University Press, 117–121, 1980.
34. **Snyder MF and Rideout VC.** Computer simulation studies of the venous circulation. *IEEE Trans Biomed Eng* 16: 325–334, 1969.
35. **Spickler JW, Kezdi P, and Geller E.** Transfer characteristics of the carotid sinus pressure control system. In: *Baroreceptors and Hypertension*, edited by Kezdi P. Dayton, OH: Pergamon, 1965, p. 31–40.
36. **Sunagawa K, Kawada T, and Nakahara T.** Dynamic nonlinear vago-sympathetic interaction regulating heart rate. *Heart Vessels* 13: 157–174, 1998.
37. **Ursino M and Magosso E.** Acute cardiovascular response to isocapnic hypoxia. I. A mathematical model. *Am J Physiol Heart Circ Physiol* 279: H149–H165, 2000.
38. **Wesseling KH and Settels JJ.** Circulatory model of baro- and cardio-pulmonary reflexes. In: *Blood Pressure and Heart Rate Variability*. Amsterdam, The Netherlands: IOS, 1993, p. 56–67.